

2012

Luminescent Nitrogen and Sulfure Adducts of CuI Disubstituted Piperazine Complexes

Jason P. Safko
College of William & Mary - Arts & Sciences

Follow this and additional works at: <https://scholarworks.wm.edu/etd>

 Part of the [Organic Chemistry Commons](#)

Recommended Citation

Safko, Jason P., "Luminescent Nitrogen and Sulfure Adducts of CuI Disubstituted Piperazine Complexes" (2012). *Dissertations, Theses, and Masters Projects*. Paper 1539626933.
<https://dx.doi.org/doi:10.21220/s2-k4bw-px13>

This Thesis is brought to you for free and open access by the Theses, Dissertations, & Master Projects at W&M ScholarWorks. It has been accepted for inclusion in Dissertations, Theses, and Masters Projects by an authorized administrator of W&M ScholarWorks. For more information, please contact scholarworks@wm.edu.

Luminescent Nitrogen and Sulfur Adducts of CuI Disubstituted Piperazine
Complexes

Jason P. Safko

Newport News, VA

Bachelor of Science, Christopher Newport University, 2010

A Thesis presented to the Graduate Faculty
of the College of William and Mary in Candidacy for the Degree of
Master of Science

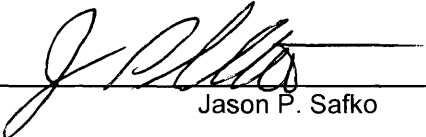
Department of Chemistry

The College of William and Mary
August, 2012

APPROVAL PAGE

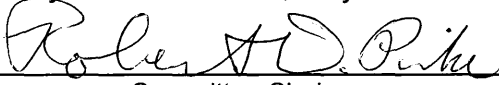
This Thesis is submitted in partial fulfillment of
the requirements for the degree of

Master of Science

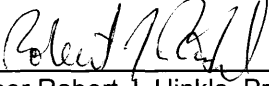


Jason P. Safko

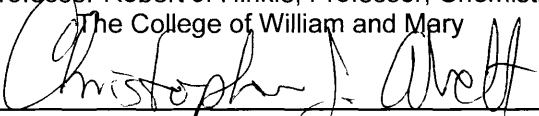
Approved by the Committee, July 2012



Committee Chair
Floyd Dewey Gottwald, Sr. Professor Robert D. Pike, Chemistry
The College of William and Mary



Professor Robert J. Hinkle, Professor, Chemistry
The College of William and Mary



Professor Christopher J. Abelt Professor (Department Chair), Chemistry
The College of William and Mary

ABSTRACT PAGE

N,N'-Disubstituted piperazine compounds were prepared and used as ligands for copper(I) iodide with the intent to produce luminescent three coordinate metal complexes. Such complexes are of interest because they have an available fourth coordination site that can allow for reaction with gaseous amines or sulfides producing an alteration in luminescence, thus making them ideal candidates for small molecule detectors. 1-Benzyl-4-ethylpiperazine (1), 1,4-dibenzylpiperazine (2), 1,4-bis(pyridin-2-ylmethyl)piperazine (3), 1,4-diphenethylpiperazine (4), 1-benzhydryl-4-benzylpiperazine (5), 1-benzhydryl-4-(pyridin-2-ylmethyl)-piperazine (6), 1,4-dimethylpiperazine (7), 1,4-diethylpiperazine (8), 1,4-diphenylpiperazine (9), and 1-benzhydrylpiperazine (10) were purchased (7–10) or synthesized (1–6) through reductive amination and characterized via X-ray crystallography and proton and carbon NMR. These piperazines were then reacted with CuI, bonding through the N and N' positions, to generate Cu(I) complexes (CuI)₂(2), (CuI)₂(3), (CuI)₂(4), (CuI)₂(6)₂, (CuI)₄(7)₂, (CuI)₂(8), and (CuI)₄(10)₄. The products were characterized by TGA, X-ray powder diffraction, and their luminescent properties were analyzed via an in-house-fabricated LED fiber optic fluorimeter. The products were all luminescent, and included both μ_2 -iodide rhomboid dimer and μ_3 -iodide cubane tetramer motifs. In many cases these oligomers were bridged to form polymeric networks. It was determined that increased size of the piperazine substituents favored the μ_2 -I rhomboid species. The photophysical behavior of the complexes was attributed to halide to ligand charge transfer (XLCT), cluster center (CC) transition, metal centered (MC), and metal to ligand charge transfer (MLCT). (CuI)₂(2) was found to form a 3-coordinate μ_2 -I polymeric system that was consistently reactive with the widest variety of gaseous amines and sulfides. This complex was also determined to be non-emissive in its unreacted form, and irreversibly generated a luminescent cubane species with replacement of the piperazine.

TABLE OF CONTENTS

Acknowledgements	iii
List of Tables	iv
Lists of Figures	v
List of Schemes	vii
List of Schematics	viii
Introduction	1
Volatile Organic Compounds	1
Copper Chemistry	3
Copper Iodide	7
Network Formation	8
Photophysics of CuI	12
Experimental	16
Materials and Methods	17
Fiber Optic LED Luminescence Spectrophotometer Construction.....	17
Schematics of Instrumentation	18
General Analysis	19
Spectroscopic Analysis	19
X-ray Crystallography	20
Powder X-ray Analysis	21
Vapor Exposure	21
Synthesis and Crystallization	21
Results and Discussion	28
Ligand Generation	28

CuI Complex Synthesis.....	37
X-ray Crystallography and CuI Complex Trends	38
Luminescence and Spectroscopy of CuI Complexes	52
Computational Results	57
Vapor Exposure Studies Using (CuI) ₂ (2), (CuI) ₂ (4), and (CuI) ₂ (8)	60
X-ray Powder Diffraction	66
Conclusion	69
References	71

Acknowledgements

I would like to extend my deepest thanks and gratitude to my graduate advisor Dr. Robert D. Pike who has greatly extended my understanding of chemical research and has also provided numerous revisions to this work. Over the past two years you have extended me every kindness while also patiently guiding me through my research, helping me grow not only as a scientist but also a person. Additionally, I would like to thank Dr. Christopher J. Abelt for not only reviewing and sitting on my committee, but also for being ready and willing to help me answer my photophysical questions and trouble shoot fluorimeter issues. I would also extend my thanks to Dr. Robert J. Hinkle for also reviewing my thesis, sitting my committee, and always reminding me that there is more to life than just work, by always bringing a great sense of humor. I would also like to acknowledge and thank my parents for all of the support and encouragement they have offered me throughout my academic career. Finally, I would like to show my gratitude to the National Science Foundation (CHE-0848109) for supporting this work.

List of Tables

<i>Table</i>	<i>Page</i>
1. Properties of Copper(I) and Copper(II).....	3
2. Disubstituted piperazine crystal and structure refinement data.....	31
3. Disubstituted piperazines selected bond lengths and angles	32
4. CuI piperazine complex crystal structure refinement data.....	39
5. CuI piperazine complex selected bond lengths and angles for all complexes	41
6. TGA copper(I) iodide complexes	45
7. CuI complex luminescence results	53
8. DFT band distances and angles of model complexes.....	59
9. Luminescent color data for (CuI) ₂ (2), (CuI) ₂ (4), and (CuI) ₂ (8).....	61
10. Luminescent emission data for nucleophile adducts of (CuI) ₂ (2) and (CuI) ₂ (8)	62

List of Figures

<i>Figure</i>	<i>Page</i>
1. Copper(II) d-shell octahedral electron configuration.....	4
2. Electron configuration of copper(I) [Ar]3d ¹⁰	6
3. π back-bonding.....	7
4. Copper iodide crystal phases	7
5. CuI complexes and networks with monodentate ligands	10
6. Bidentate ligand bridged networks	11
7. Copper(I) iodide luminescence spectra.....	12
8. Proposed 3-coordinate (CuI) ₂ (LL) polymer.....	14
9. Synthesized and purchased disubstituted piperazine ligands	16
10. Cross-section of six around one fiber-optics.....	18
11. ORTEP plot of disubstituted piperazines 5 , 6 , 2 , 3 , 4 , and 9	34
12. Disubstituted piperazine overlay of substituent orientation	35
13. Short contact interaction for ligand species 2 and 4	37
14. 3-coordinate CuI framework and (CuI) ₂ (Phenazine)	39
15. X-ray structures of (CuI) ₂ (3), (CuI) ₂ (4), and (CuI) ₂ (5)	43
16. X-ray structure of (CuI) ₄ (7) ₂	44
17. TGA trace of (CuI) ₂ (7), (CuI) ₂ (8), (CuI) ₂ (2), and (CuI) ₂ (4).....	45
18. X-Ray structure of (CuI) ₄ (10) ₄	47
19. X-Ray structure of (CuI) ₅ (10) ₄	47
20. TGA trace of (CuI) ₅ (10) ₄ and (CuI) ₄ (10) ₄	49
21. X-ray structures of (CuI) ₂ (3) polymer chain and (CuI) ₂ (6) dimer	51

22. TGA trace of $(\text{CuI})_2(\mathbf{3})$ and $(\text{CuI})_2(\mathbf{6})$	52
23. Luminescence excitation and emission spectra of $(\text{CuI})_4(\mathbf{7})_2$ and $(\text{CuI})_4(\mathbf{10})_4$	53
24. Luminescence excitation and emission spectra of $(\text{CuI})_2(\mathbf{4})$ and $(\text{CuI})_2(\mathbf{8})$	55
25. Luminescence excitation and emission spectra of $(\text{CuI})_2(\mathbf{2})$	55
26. Luminescence excitation and emission spectra of $(\text{CuI})_2(\mathbf{3})$ and $(\text{CuI})_2(\mathbf{6})$	57
27. Computational 3 and 4-coordinate models	58
28. Excitation DFT orbital model of $(\text{CuI})_2(\text{NMe}_3)_2$, \mathbf{Y}	59
29. Excitation DFT orbital model of $(\text{CuI})_2(\text{DMP})_2$, \mathbf{Z}_1 and \mathbf{Z}_2	60
30. Vapor exposure emission spectra $(\text{CuI})_2(\mathbf{8})$ and $(\text{CuI})_2(\mathbf{2})$	63
31. Luminescence response of Nu-exposed $(\text{CuI})_2(\mathbf{8})$	64
32. Luminescence response of Nu-exposed $(\text{CuI})_2(\mathbf{2})$	65
33. PXRD diffractogram overlays of $(\text{CuI})_2(\mathbf{3})$ and $(\text{CuI})_2(\mathbf{4})$	66
34. PXRD diffractogram overlays of $(\text{CuI})_2(\mathbf{2})$, $(\text{CuI})_2(\mathbf{6})$, and $(\text{CuI})_2(\mathbf{8})$	67
35. PXRD diffractogram overlays of $(\text{CuI})_2(\mathbf{8})$, $(\text{CuI})_2(\mathbf{8})$ 5% pyridine/toluene, and $(\text{CuI})_4\text{Py}_4$..	68

List of Schemes

<i>Scheme</i>	<i>Page</i>
1. CuX structural motifs.....	9
2. Piperazine substituents	29
3. Reductive amination reaction	30
4. Reductive amination mechanism	30
5. Resonance structure of 1,4-diphenylpiperazine	36

List of Schematics

<i>Schematics</i>	<i>Page</i>
1. LED fiber optic fluorimeter	18
2. LED light source enclosure	19
3. Circuit diagram of light source	19

INTRODUCTION

Volatile Organic Compounds.

Volatile organic compounds (VOCs) are defined as organic chemicals that have a high vapor pressure at standard temperature and pressure (STP) as a result of their low boiling points. VOCs are also emitted from a variety of compounds including solids and liquids. The EPA defines a VOC by what is not, stating that a VOC is 'any compound of carbon, excluding carbon monoxide, carbon dioxide, carbonic acid, metallic carbides or carbonates, and ammonium carbonate, which participates in atmospheric photochemical reactions.'¹ They go on to further list a series of volatile compounds that have been determined to have negligible photochemical reactivity and are relatively safe.¹ VOCs are usually liquids or gases and are generated from a prolific number of sources ranging from everyday household products to mass manufacturing processes. Some examples include paints and lacquers, cleaning supplies, pesticides, glues and adhesives, office equipment such as copiers and printers, even correction fluids and permanent markers.

Due in large part to their high volatility, VOCs can represent a serious health risk to humans. Their toxicity ranges from species that are mere irritants to the eyes, nose, and throat causing nausea and headaches, to those that are known cancer agents, and can cause damage to the liver, kidneys, and central nervous system. Furthermore, the extent of the health effects caused by VOCs can be linked to the degree of exposure. Although some VOCs are toxic irrespective of exposure concentration, others are only toxic above a certain threshold, whether exposure happens all at once or over a long period of time. Extended exposure can cause normally benign VOCs to become exponentially more dangerous when they are produced in a confined space, thereby greatly increasing the delivered dose. Furthermore, VOC-related

illnesses can often go unnoticed or misdiagnosed, because VOC exposure may be occurring at relatively low concentrations. Therefore, given the prevalence of these potentially toxic compounds in such close proximity to humans, there is a significant need for practical VOC detectors that can be applied in both open and closed environments.

A variety of general detection methods already exist for VOCs, each with their own advantages and disadvantages. One of the techniques in common use is gas chromatography/mass spectrometry (GC/MS), however, this technique is technologically complex, requiring the use of high vacuum. Therefore, GC/MS is currently difficult to take into the field and requires trained personnel to operate. Another more promising type of volatile gas sensor incorporates a networked chemical substrate layer designed to interact with the gaseous compounds, resulting in an analytical response, be it electronic or visual. This effect is normally achieved through any of four principal chemical mechanisms: absorption, physisorption, chemisorption, or coordination chemistry.² Depending on the mechanism chosen, the selectivity and reversibility of the chemical interaction between the analyte and the substrate layer is strongly influenced. The phenomenon of absorption does not involve a true chemical reaction, but instead involves the inclusion of the analyte into the porous network of the substrate, allowing for a highly reversible, but not particularly selective, process. Physisorption is also a physical process, in which van der Waals interactions induce analyte binding to the substrate surface, giving a highly reversible and extremely nonselective interaction. Chemisorption is a related surface chemical process in which the chemisorbate reacts with the detector substrate, usually through sharing of an electron lone pair. This process is normally very selective and is potentially reversible, depending on the binding strength of both the substrate and the chemisorbate. Finally, coordination chemistry makes full use of metal-ligand bonding, although steric and electronic factors can influence binding strength and

reversibility. The ideal gas sensor would make use of one or more of these substrate-analyte interaction mechanisms, while also involving minimal expense, and offering rapid, reversible, and analytically accurate analysis results.

Copper Chemistry.

Recent work has shown that copper chemistry may open up new avenues in which new detector substrates could be generated.³ Copper exists in three common oxidation states: Cu(0) $[\text{Ar}]3d^{10}4s^1$, Cu(I) $[\text{Ar}]3d^{10}$, and Cu(II) $[\text{Ar}]3d^9$ (see **Table 1**). As is the case with most metals, copper(0) chemistry is generally limited to redox activity, because of the relatively higher stability of the Cu(I) and Cu(II) ions. Furthermore, copper(0) would be of limited utility as a detector because its properties are greatly limited to sorptive and physisorptive interactions with incoming analytes.

Table 1. Properties of Copper(I) and Copper(II)

Properties	Copper(I)	Copper(II)
Electron Configuration	$[\text{Ar}]3d^{10}$	$[\text{Ar}]3d^9$
Possible Geometries	<ul style="list-style-type: none"> • 4-Coordinate Tetrahedral • 3-Coordinate Trigonal Planar • 2-Coordinate Linear 	<ul style="list-style-type: none"> • 6-Coordinate Distorted Octahedral • 5-Coordinate Pyramidal • 4-Coordinate Square Planar
Photophysical Behavior	Metal-centered or metal to ligand charge transfer	Intra-d-subshell transitions most important
Compound Colors	White / Colorless	Green / Blue Salts
Magnetic Properties	Diamagnetic	Paramagnetic
Lewis Acid Type	Soft	Intermediate

Copper(II) is found in simple ionic salts, such as copper(II) sulfate and copper(II) chloride, or in coordination complexes. The coordination environments most often associated with copper(II) are either 6-coordinate distorted octahedral, 5-coordinate pyramidal, or 4-coordinate square planar metal complex geometries, **Table 1**. These geometries result from the incomplete d-subshell causing significant crystal field stabilization to occur. According to crystal field theory, all of the d-orbitals will be destabilized by the incoming ligands through electrostatic effects. However, some orbitals are more destabilized than others causing preferential population of the d-orbitals so as to minimize destabilization. Furthermore, notable distortion of the coordination spheres having degenerate ground states (especially the octahedral field) is observed due to the Jahn Teller effect. According to the Jahn Teller principle, the normal octahedral configuration is rearranged so as to remove ground state degeneracy, **Figure 1**.

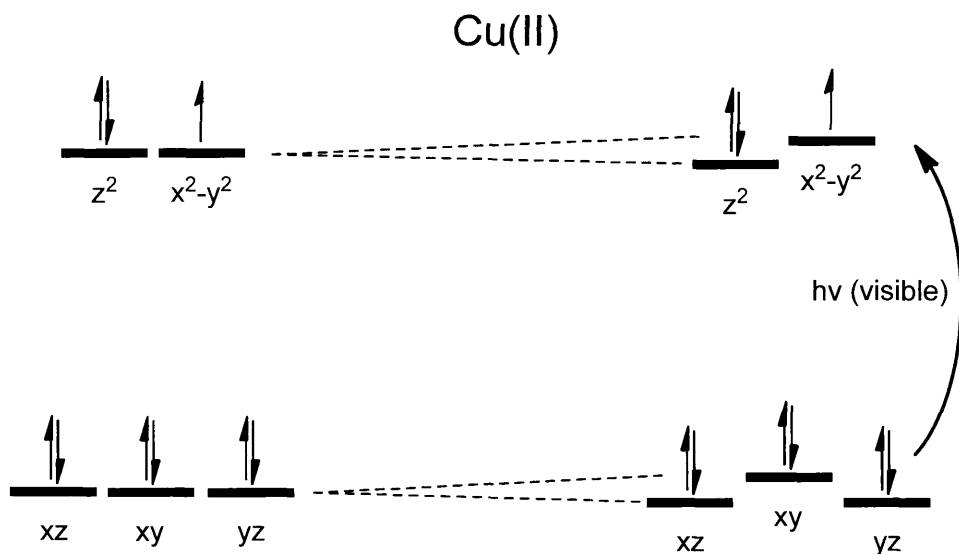


Figure 1. Copper(II) d-shell octahedral electron configuration, demonstrates Jahn Teller distortion in order to alleviate ground state degeneracy, and further offers paramagnetism and intra-d-subshell visible light absorption in the red/orange region.

Copper(II) complexes have interesting magnetic, absorptive, and electrochemical properties.^{4,5} To achieve the 2+ oxidation state, the remaining electron in the 4s subshell must

be lost, along with a single electron from the 3d. This vacancy in the 3d-shell enables absorption of photons with frequencies in the visible region of the electromagnetic spectrum, specifically the red/orange, imparting to Cu(II) complexes their blue or green color. Similarly, the single unpaired electron gives Cu(II) its characteristic paramagnetic properties, wherein the unpaired electrons will align with an applied magnetic field. The higher oxidation state further contracts the Cu^{2+} ionic radius, making Cu(II) a harder Lewis acid than Cu(I) and therefore less likely to interact with soft Lewis bases that typically contain unsaturated N, S, and P donor sites, and more likely to coordinate with hard bases that feature saturated N or O donors.

Copper(I) brings a variety of interesting properties to the table. It is well documented to be a low-coordinate metal complex former, have significant photoluminescent properties under long wavelength UV irradiation, and to produce labile d^{10} complexes.³ Cu(I) offers a flexible coordination sphere creating three different low-coordinate geometries: 4-coordinate tetrahedral, 3-coordinate trigonal planar, or 2-coordinate linear systems, **Table 1**. The flexible low-coordinate geometries of Cu(I) are influenced by its outer valence electron configuration, wherein the single electron is lost from the 4s shell, yielding a full 3d subshell, **Figure 2**. Due to its lack of crystal field stabilization, Cu(I) is not particularly obedient to the 18 electron rule, beyond allowing a maximum of only four ligands to coordinate. This is because when the 3d subshell is completely filled, the electrostatic destabilization caused by the incoming ligands is rendered moot. Moreover, with a full 3d subshell, the average energy of each subshell is maintained under all coordination geometries; therefore preferential population of the orbitals through crystal field stabilization cannot occur.

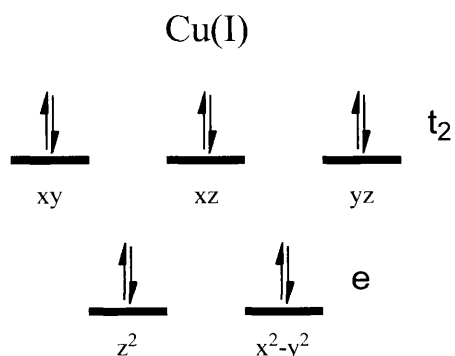


Figure 2. Electron configuration of copper(I) $[\text{Ar}]3d^{10}$. The filled d-subshell electron configuration $[\text{Ar}]3d^{10}$ for copper(I) prevents crystal field preferences and intra-d-subshell transitions. Tetrahedral geometry is shown.

Furthermore, with the filled 3d subshell, there are no d to d transitions, as seen with Cu(II). Therefore, the observed transitions occur mainly in the UV region, unless the π or π^* orbitals of the ligand lie sufficiently low that a lower energy visible transitions can take place. These are associated with either metal-centered 3d to 4s/4p transitions (MC) or metal to ligand charge transfer (MLCT). Finally, this d^{10} configuration also offers the ability for Cu(I) to demonstrate very labile interactions toward coordinated ligands. Tetrahedral Cu(I) has low energy e orbitals and higher energy t_2 orbitals, all of which are filled, **Figure 2**, providing an even distribution of electron density throughout the d-orbitals, obviating any crystal field effects. In lieu of crystal field effects, the coordination environment of Cu(I) is determined solely by its relative electrophilicity (which is fairly low given its univalent charge and large ionic radius), and steric demand of the ligands. This results in relatively labile ligands in Cu(I) complexes.

The relatively large ionic radius of Cu(I) causes it to act as a soft acid with a relatively polarizable electron cloud favored by soft Lewis bases. Such soft Lewis bases act as π -backbonders, both donating electron density to the metal center through σ -donation and also receiving electron density back from the metal into vacant π^* -orbitals, **Figure 3**. This enhances

the affinity of Cu(I) for the soft P-, S-, and unsaturated N-containing ligands (VOCs), but not hard saturated nitrogen- or oxygen-based ligands.

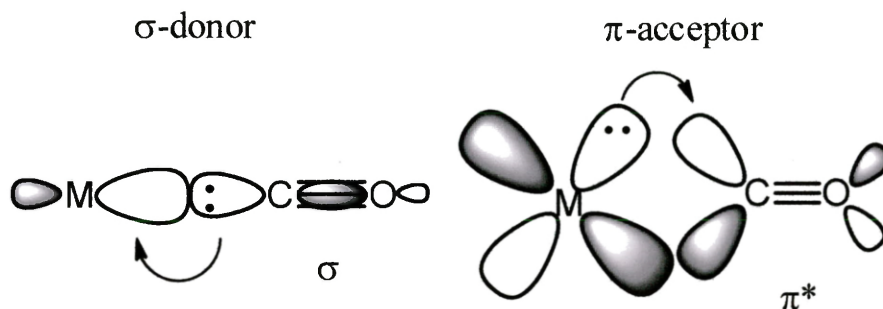


Figure 3. π back-bonding. Electron density from the ligand HOMO is donated to the metal center through σ -donation interactions, and electron density from the metal is π back-donated to the ligand LUMO, as illustrated for a metal carbonyl interaction.

Copper Iodide.

Copper(I) iodide (CuI) is the most stable Cu(I) halide salt because iodide is the softest, most oxidizable, and least reducible halide, and therefore stabilizes the readily oxidizable Cu(I) cation. CuI exists in three major crystalline phases: zinc blend face centered cubic (γ -CuI) below 369°C, wurtzite hexagonal close packing (β -CuI) between 369-407°C, and simple cubic (α -CuI) above 407°C, **Figure 4**.

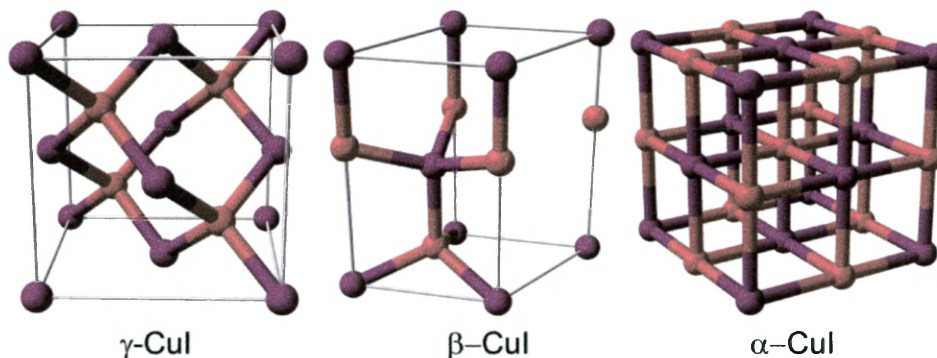
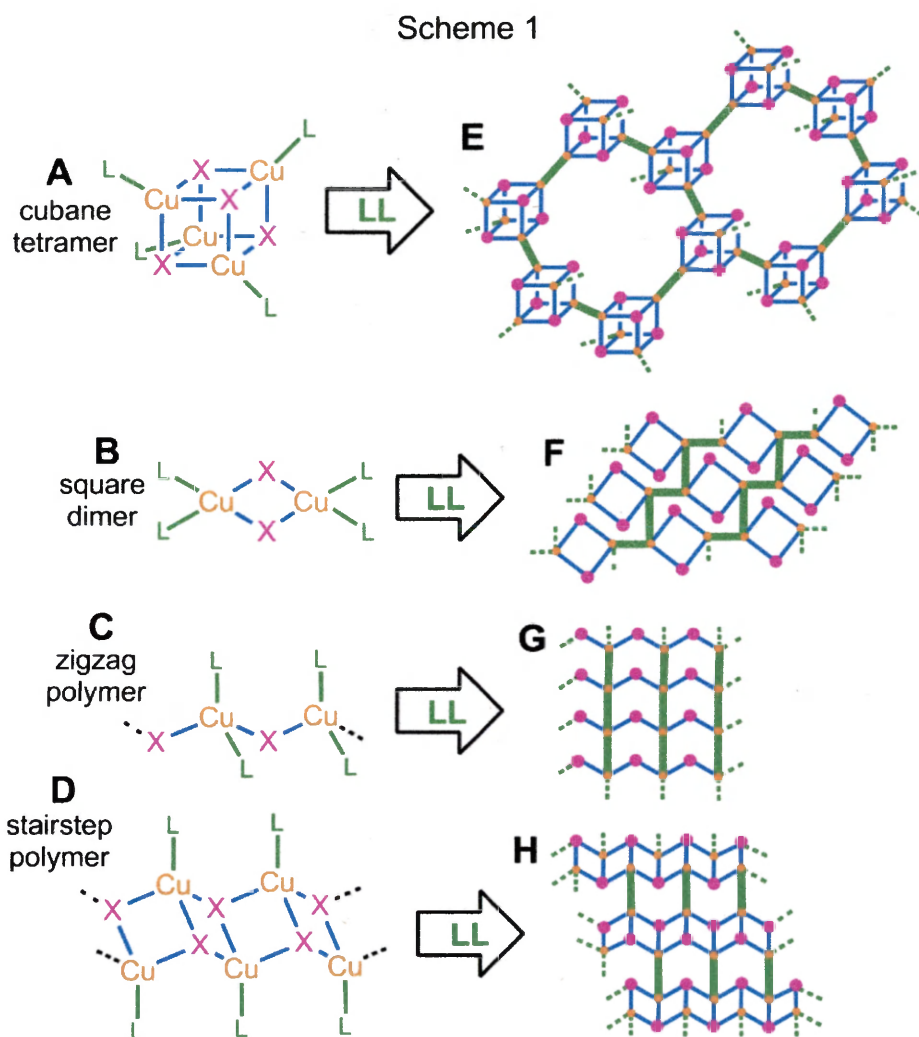


Figure 4. Copper iodide crystal phases. (γ -CuI) low temperature face centered cubic or zinc blend structure, (β -CuI) mid temperature wurtzite, and (α -CuI) high temperature rock salt orientation.

In the α phase, copper ions occupy all of the octahedral holes in a cubic closest packed arrangement of iodide ions. In the β and γ phases, however, Cu^+ sits in half of the tetrahedral interstices of closest packed iodide lattices. In the former, iodides are hexagonally closest packed, while in the latter they are cubic closest packed. In either case a relatively simple lattice network results, with 4-coordinate copper and iodide atoms bonded 2.338 Å apart.

Network Formation.

Copper(I) is a robust network former, preferring low 2-, 3-, or 4-coordinate environments. The coordinative flexibility of Cu(I) and the variable bridging modes of halide ($X = \text{Cl}^-$, Br^- , or I^-) are illustrated in the diversity of CuX structural types found with simple monodentate ligands (L) shown on the left-hand side of **Scheme 1**. This diversity is further expanded through the use of bidentate ligands (LL), see **Scheme 1**, right hand-side. When monodentate or capping ligands are introduced to CuX, μ_2 - or μ_3 -halide bridging of Cu(I) centers may be found. The μ_2 -mode is seen in **B** and **C**, **Scheme 1**, wherein Cu(I) centers are bonded to two bridging halides. In contrast, the μ_3 -bridging mode is observed in systems **A** and **D** wherein three Cu(I) centers are linked by triply-bridging halide ligands. Furthermore, both μ_2 -X and μ_3 -X allow for the generation of small dimers or tetramers and polymeric systems.



Let us consider iodide as our halide. Although μ_2 -I and μ_3 -I bridging are most common, iodide is capable of forming 1-, 2-, 3-, or 4-coordinate metal bonding modes, permitting the generation of various networks. As a result, a great many simple monodentate N-, S-, and P-donor complexes of CuI are known.⁴ These structures are typically based on any of four motifs (see **Scheme 1**): the rhomboid Cu_2I_2 dimer, the cubane Cu_4I_4 tetramer (or occasionally higher order clusters, such as Cu_6I_6), or the infinite $\text{Cu}_\infty\text{I}_\infty$ zigzag or stair step polymers, see **Figure 5 (A-D)**.

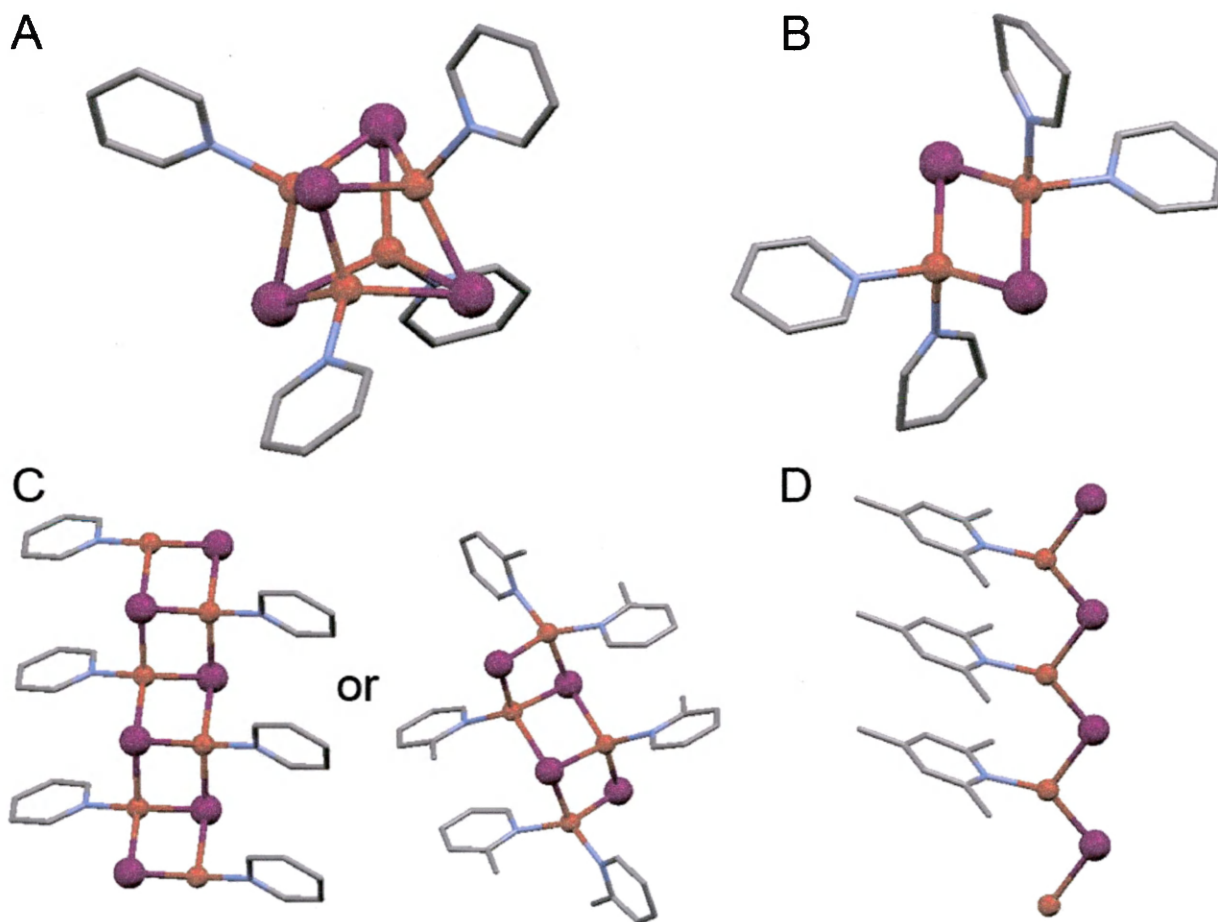


Figure 5. CuI Complexes and Networks with Monodentate Ligands: A) CuI pyridine cubane,^{6a} B) CuI pyridine square dimer,^{6b} C) CuI pyridine and CuI 2-methylpyridine ladders,^{6c, 6d} and D) CuI 2,4,6-trimethylpyridine zig-zag.^{6e}

When bidentate ligands (LL) that cannot chelate due to ring constraints, such as piperazine (H₂Pip) and 1,4-diazabicyclo[2.2.2]octane (DABCO), are utilized, a bridging effect is observed. Cross-linking of Cu_nI_n knots or chains opens up a wide variety of network structures, see **Scheme 1 (E – H)**. Examples of each type of network are known: (CuI)₄(LL)₂ type **E**,^{7,8} (CuI)₂(LL)₂ type **F**,^{8j,8k,8n,9} CuI(LL) type **G**,^{9a,9b,10} and (CuI)₂(LL) type **H**.^{9a,9b,10a,10b,11}, **Figure 6**.

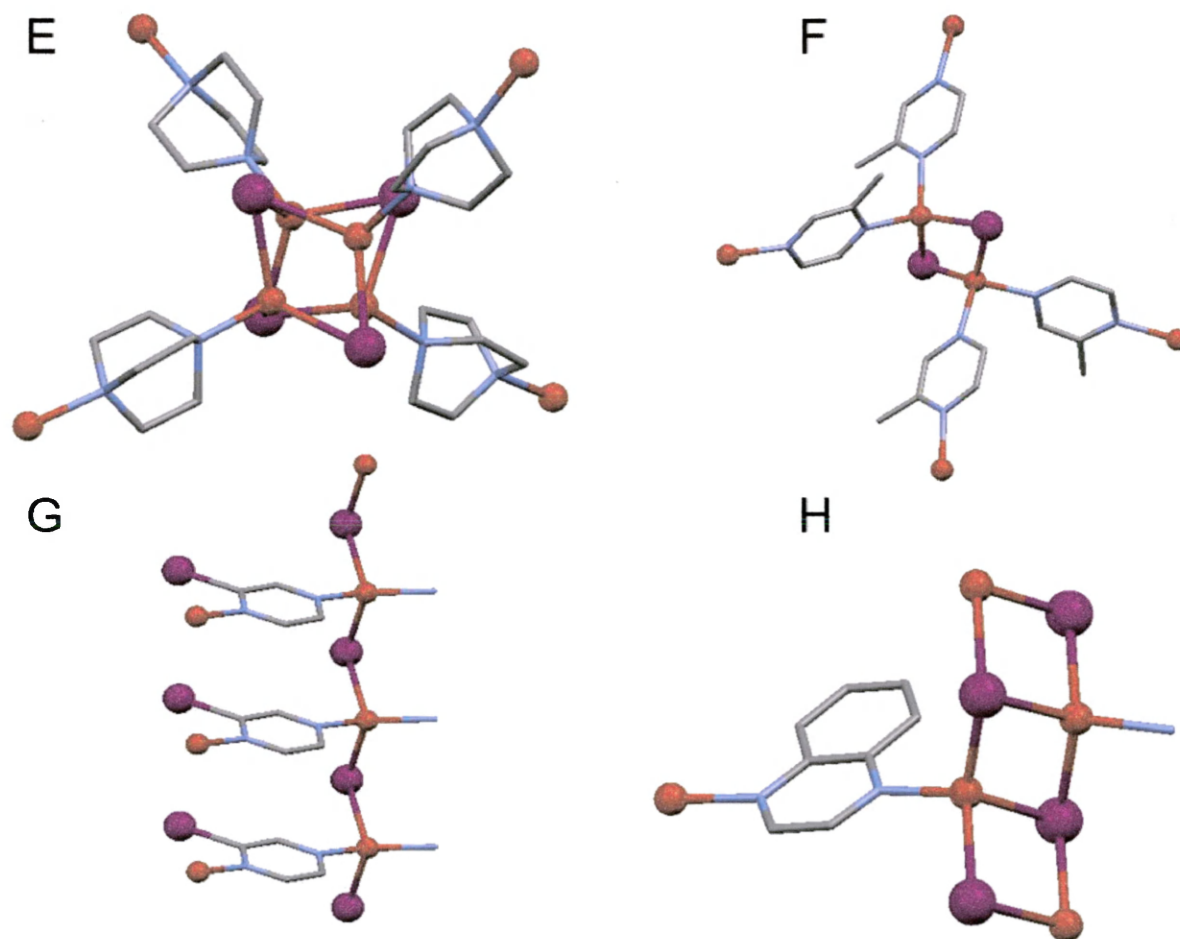


Figure 6. Bidentate Ligand Bridged Networks: A) CuI DABCO cubane network, B) CuI 2-methylpiperazine square dimer network, C) CuI 2-iodopiperazine zig-zag network, D) CuI quinoxaline ladder network.

Consequently, network formation in copper iodide is very susceptible to steric influence via the coordinating ligands. This, more than anything else, can be manipulated to force the metal center to adopt different coordinative geometries. For example, one might be able to create a potential nucleophile detector by forcing the copper center into a system wherein a coordinative vacancy is found. This vacancy could act to spontaneously pick up a nucleophile from the environment. Unfortunately, the previous described structures (**A-H**) are all 4-coordinate, and therefore have no coordinative vacancies for the uptake of nucleophiles or VOCs. However, if these same structures (**A-H**) could be forced into forming 3-coordinate Cu(I)

centers by manipulating the nature of the ligand, the open coordinative vacancy could allow for facile reaction with an incoming nucleophile. However, even if such a reaction were to occur, it would need to be detectable in some way.

Photophysics of CuI.

In its pure form, copper(I) iodide shows luminescence centered near the UV/Vis border, appearing as a blue or purple emission, **Figure 7**.

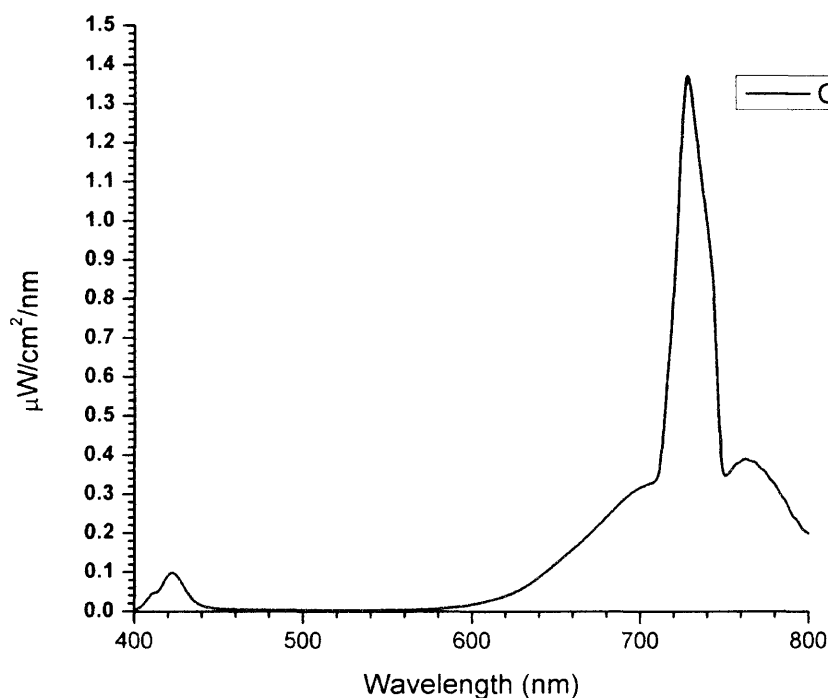


Figure 7. Copper(I) iodide luminescence image under 365 nm irradiation.

However, this emission changes greatly when CuI is reacted with ligands such as piperazine or pyridine which force CuI into $\text{Cu}_4\text{I}_4\text{L}_4$ clusters. The luminescence emission that results typically exhibits a low energy (LE) band, resulting from cluster centered transitions. These transitions emanate from a combination of two electronic processes: halide to metal charge transfer (XMCT) and metal centered charge transfer (MCCT).¹² The XMCT emission is a result of

electrons relaxing after excitation from a largely halide-based highest occupied molecular orbital (HOMO) to a largely metal-based lowest unoccupied molecular orbital (LUMO). In particular, the HOMO is a hybrid of >80% iodide 5p and <20% copper 3d orbitals. The LUMO is significantly simpler insofar as it is almost purely comprised of copper 4s orbital, resulting in the observed XMCT being largely iodide (I) 5p to copper (Cu) 4s. The other component of the LE emission is generated due to MCCT wherein electrons transition between a Cu 3d-orbital-based HOMO, and 4s-orbital-based LUMO. Furthermore, it is believed that these transitions occur simultaneously and non-preferentially throughout the CuI cluster. This is due to electron reorganization effects creating a hybrid configuration of both emission types delocalized throughout the Cu₄I₄ cluster center.

Different ligands not only change the CuI network type, but more significantly modify the photophysical properties of the overall complex. This adaptation to the photoactivity of the complex is attributed to the generation of a HE emission band caused by halide to ligand charge transfer (XLCT). In this case, the HE band is formed by electrons relaxing from the above-described hybrid 5p/3d HOMO of the CuI cluster to π^* orbitals of the ligand.¹² Furthermore, this HE emission band is very dependent on the nature of the ligands, because each ligand brings with it different electronic properties that influence the environment in which the XLCT occurs. For example, XLCT is more energetically favorable for ligands having π systems, such as aromatics. These environmental changes then manifest themselves as different emission wavelengths.

Interestingly, the HE and LE emission bands are seen to be independent of one another. For instance, considering (CuI)₄Py₄ as an example of an XLCT complex, (**Figure 5**), a large Stokes shift is observed for the LE band and a small one is identified for the HE band. For our purposes,

the Stokes shift is merely the difference between the emission and excitation maxima of the $(\text{CuI})_4\text{Py}_4$ complex. This larger Stokes shift for the LE emission can be explained based upon a sizeable amount of photophysical energy being required for MCCT distortion of the CuI cluster through contraction of the Cu_4 core and expansion of the I_4 core necessitated by greater Cu–Cu bonding in the excited state. Conversely, the smaller Stokes shift of the HE band results from the lack of significant distortion of the CuI cluster. Thus, the LE band is not significantly affected by the electrical environment of the ligand whereas the HE band is found to be somewhat red shifted in the case of dimers. Furthermore, the HE band is highly affected and results in a variety of different emission colors dependent on the coordinated ligand, adding more credence to the independent nature of these two emission bands.

Keeping these principles in mind, if one could form the earlier discussed 3-coordinate planar CuI system through the use of bridging ligands (LL) similar to those in **Figure 8**, the LE XMCT and CCCT could be eliminated by cutting the CuI cubane in half.

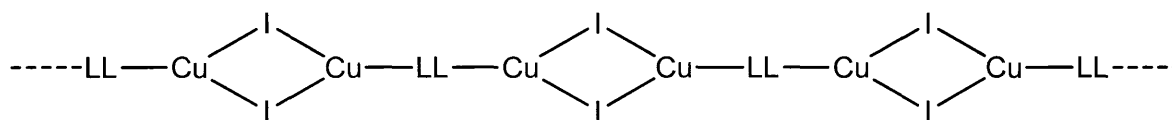


Figure 8. Proposed 3-coordinate $(\text{CuI})_2(\text{LL})$ polymer to be used in sensor applications.

This in turn offers a system that conceivably has a HE emission band that would remain constant depending on the nature of the LL ligand, and then become red shifted by an incoming nucleophile. Moreover, the coordinating VOC would then create an emission with a specific fingerprint unique to that VOC. Therefore, we set out to use steric control to force copper iodide into forming linear 3-coordinate chains that would be receptive to incoming nucleophiles

and change the luminescence of the complex accordingly. Such a strategy seemed to offer potential for a luminescence-based detection system for nucleophilic substrates.

EXPERIMENTAL

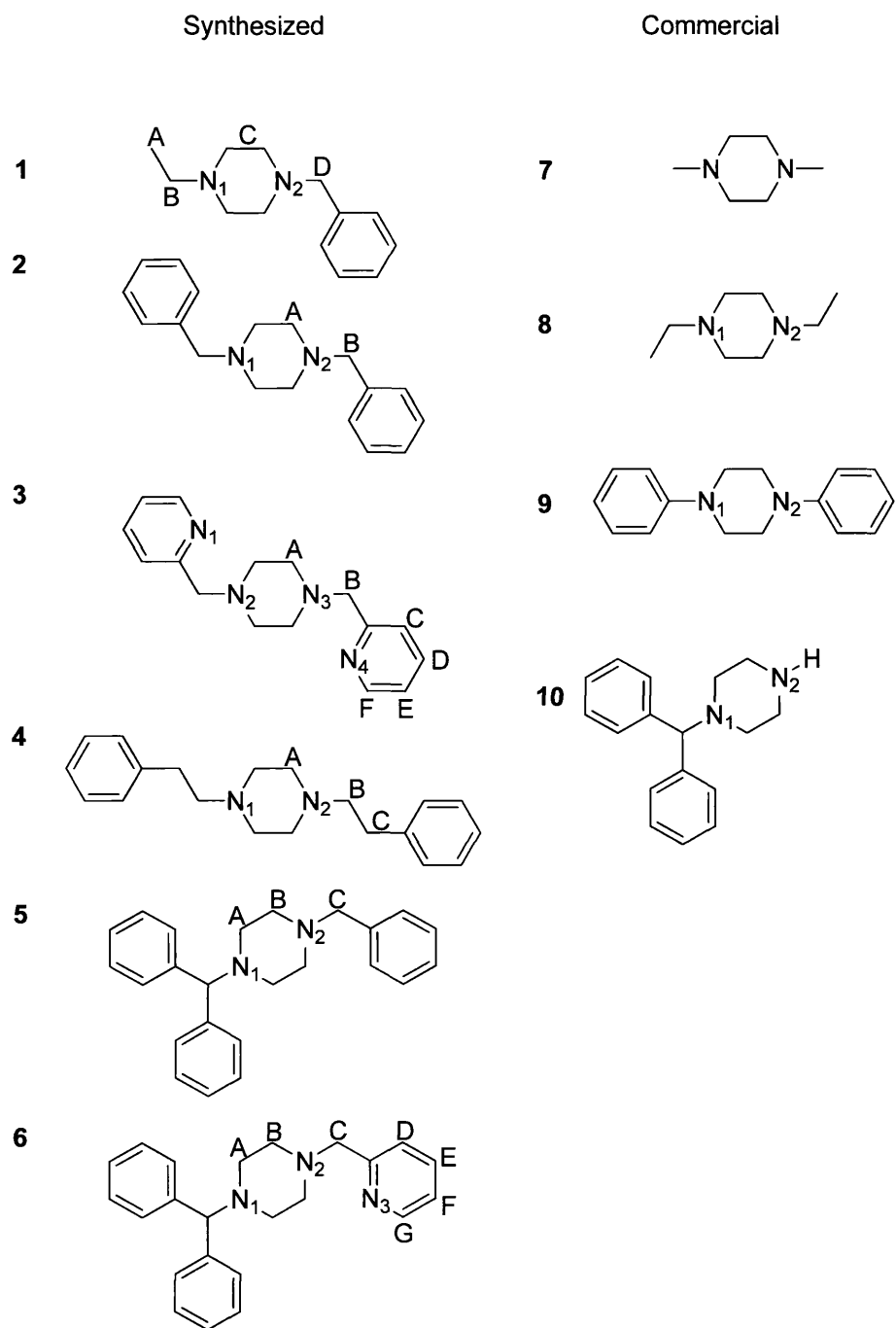


Figure 9. Synthesized (1-6) and purchased (7-10) disubstituted piperazine ligands.

Materials and Methods.

All reagents were purchased from Aldrich or Acros and used without purification, except for ligands **1**, **2**, **3**, **4**, **5**, and **6** which were prepared using modified literature methods.¹¹

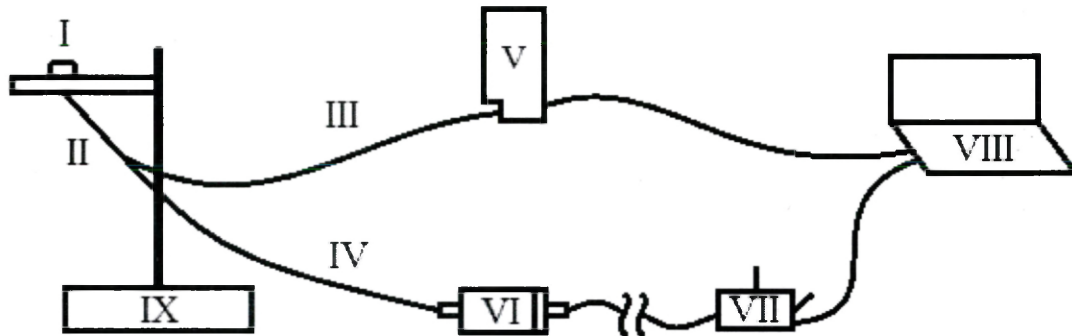
Fiber Optic LED Luminescence Spectrophotometer Construction.

The 1000 μm optical grade fiber-optic cables were cut into seven equal lengths. The detector fiber was then split off and sheathed completely in aluminum, to minimize leakage of light into the fiber. The detector fiber was then bundled with the other six fibers in a hexagonal close packing formation with the detector fiber as the central fiber, **Figure 10**. The seven fiber bundle was then sheathed in a fluorinated ethylene propylene (FEP) tubing, for about the first six inches to a foot (**Schematic 1, II**). Next, the detector fiber was separated from the bundle, sheathed similarly in FEP (**Schematic 1, III**) and later connected to the detector. The resulting six fibers were also sheathed in FEP (**Schematic 1, IV**), and later run to the excitation source. Finally, the whole system was clad in heat shrink tubing in order to minimize light leakage into, and out of the fiber-optic system, being careful not to overheat the fiber-optics, so as to avoid heat degradation. Once insulate, all three ends of the fiber-optics were polished to optical grade smoothness using optical sand paper of grits 0.5 μm , and 1 μm working one's way up in grit.

The six polished excitation fibers were then connected to the 365 nm LED source enclosure (**Schematic 1, VI**), expansion of enclosure shown in (**Schematic 2**). Power was then run from the laptop to the source enclosure by repurposing a USB cable and creating a buffer circuit shown in schematic 3, and enclosing the circuit in an aluminum circuit box (**Schematic 1, VII**). Conversely, the polished detector fiber was run to the Ocean Optics USB 2000+ detector

(Schematic 1, V). The raw luminescence data was then interpreted by Ocean Optics Spectra Suite in absolute irradiance mode allowing for both the intensity and wavelength of the luminescence peak to be measured.

Schematics of Instrumentation.



Schematic 1: (I) sample holder, (II) six around one fiber-optics, (III) central detector fiber separated from six excitation fibers, (IV) six excitation fibers, (V) USB 2000+ Ocean Optics detector, (VI) excitation source enclosure, (VII) on/off and excitation source attenuator, (VIII) laptop data analysis, and (IX) sample stand and instrument support.

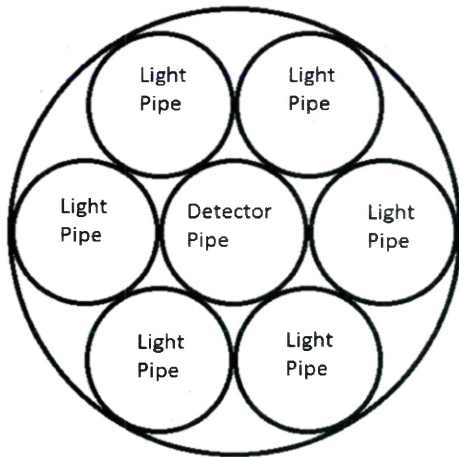
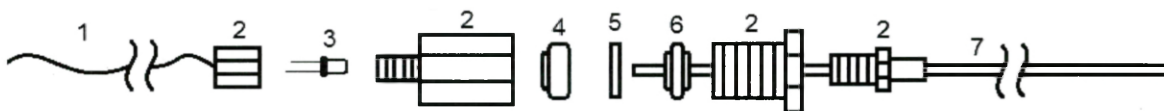
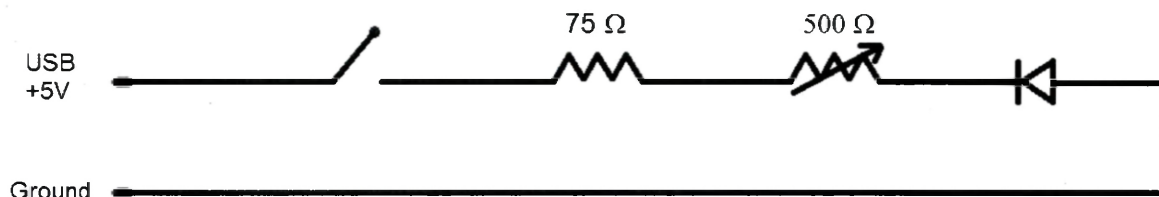


Figure 10: Cross-section of six around one fiber-optics.



Schematic 2: (1) LED power source, (2) swagelok fittings making up the enclosure, (3) Nichia 365 nm pot LED, (4) supports and centering washers for LED, (5) shemrock 365 nm line filter, (6) support and centering washers for fiber-optics, (7) six bundled excitation fibers.



Schematic 3: Circuit Diagram of VII in **schematic 1**

General Analysis.

Analyses for C, H, and N were carried out by Atlantic Microlabs, Norcross, GA or using a Thermo Scientific Flash 2000 Organic Elemental Analyzer with a Mettler Toledo XP6 Microbalance. Thermogravimetric analyses (TGA) were conducted using a TA Instruments Q500 in the dynamic (variable temp.) mode with a maximum heating rate of 50 °C/min. to 300 °C under 60 mL/min. N₂ flow. NMR data were recorded on a Varian Mercury 400 instrument (s = singlet, d = doublet, t = triplet, br = broad, Ph = phenyl, Py = pyridyl).

Spectroscopic Analysis.

Spectroscopic measurements on CuI-piperazine complexes were made at the University of Maine using the following equipment: Steady-state photoluminescence spectra of the complexes were recorded with a Model QuantaMaster-1046 photoluminescence spectrophotometer from Photon Technology International. The instrument is equipped with two

excitation monochromators and a single emission monochromator with a 75W xenon lamp. Low temperature steady-state photoluminescence measurements were achieved by using a Janis St-100 optical cryostat equipped with a Honeywell temperature controller. Liquid nitrogen was used as coolant. Lifetime measurements were conducted using an Opolette™ (HE) 355 II UV tunable laser with a range of 210–355 nm. The laser has a Nd:YAG flashlamp pumped with a pulse repetition rate of 20 Hz and an average output power 0.3 mW. The detection system is composed of a monochromator and photomultiplier from a Jobin Yvon Ramanor 2000M Raman spectrometer. Data were collected by a Le Croy 9310C dual 400 MHz oscilloscope. The decays were averaged over 1000 sweeps and fitted using a curve fitting method in Igor Pro 6.0. Spectroscopic measurements on CuI-piperazine-nucleophile adducts were carried out using the fiber optic LED spectrophotometer system described above.

X-ray Crystallography.

Crystals were mounted on glass fibers. All measurements were made using graphite-monochromated Cu K α radiation on a Bruker-AXS three-circle diffractometer, equipped with a SMART Apex II CCD detector. Initial space group determination was based on a matrix consisting of 120 frames. The data were reduced using SAINT+,¹³ and empirical absorption correction applied using SADABS.¹⁴

Structures were solved using direct methods. Least-squares refinement for all structures was carried out on F^2 . The non-hydrogen atoms were refined anisotropically. Hydrogen atoms were located in the Fourier difference map and then allowed to refine isotropically. Structure solution, refinement and the calculation of derived results were performed using the SHELXTL

package of computer programs.¹⁵ Details of the X-ray experiments and crystal data are summarized in **Table 1**. Selected bond lengths and bond angles are given in **Table 2**.

Powder X-ray Analysis.

Powder diffraction analysis was carried out on a Bruker *SMART Apex II* diffractometer using graphite-monochromated Cu K α radiation. Well-ground powder samples were milled with Paratone N oil. Four frames were collected, covering a 2 θ range of 5–100°. The data were processed using *DIFFRAC-Plus* and *EVA* software.

Vapor Exposure.

Vapor exposures were performed in a lidded 9.5x5.0x5.5 cm amber jar. The atmosphere within the jar was then saturated with one of nineteen VOC's by adding enough VOC to the jar that there was liquid collecting in the bottom. A one dram vial with about 0.12 g of (CuI)₂(N,N'-Diethylpiperazine), (CuI)₂(N,N'-Dibenzylpiperazine), or (CuI)₂(N,N'-bis-Phenethylpiperazine) was then placed within the jar and exposed for 10 min. After exposure the one dram vial was removed with large forceps and any excess VOC was removed from the vial by degassing with Ar/N.

Synthesis and Crystallization.

1,4-Diphenylpiperazine (9):

Commercial **9** (0.477 g, 2.00 mmol) was heated with CuI (0.190 g, 1 mmol) in 30 mL MeCN solution to 100 °C for 3 d in a sealed tube. No reaction took place, but **9** recrystallized, forming X-ray quality crystals.

1-benzy-4-ethylpiperazine (1):

1-ethylpiperazine (1.140g, 9.985 mmol) and phenylacetaldehyde (1.063 g, 8.848 mmol) were dissolved in 40 mL of CH₂Cl₂ and stirred under Ar at room temp. To this solution a few drops of trifluoroacetic acid (0.2 mL) were added, and the mixture was allowed to stir for 30 min, producing a clear yellow solution. Next, NaBH(OAc)₃ (2.116 g, 9.984 mmol) dissolved in 15 mL CH₂Cl₂ was added, and the solution allowed to stir overnight under Ar. The resulting solution was washed with 1 M NaOH (aq), then saturated NaHCO₃ (aq), and finally deionized water. The organic layer was then evaporated in vacuo, producing a yellow oil. ¹H NMR (400 MHz, CDCl₃) δ 1.07 (t, J=7.2 Hz, 2H, CH₂^B), 2.41 (q, J=7.2 Hz, 3H, CH₃^A), 2.45 (s, 8H, CH₂^C), 2.48 (s, 2H, CH₂^D), 7.30 (m, 5H, CHPh). ¹³C{¹H} NMR (100 MHz, CDCl₃): δ 12.24, 52.54, 53.06, 53.32, 63.324, 127.20, 128.40, 129.44, 138.40.

1,4-Dibenzylpiperazine (2):

Piperazine (0.813 g, 10.00 mmol) and benzaldehyde (2.121 g, 20.00 mmol) were dissolved in 30 mL of CH₂Cl₂ and stirred under Ar at room temperature. To this solution a few drops of trifluoroacetic acid (0.2 mL) were added, and the mixture was allowed to stir for 30 min, producing a clear yellow solution. Next, NaBH(OAc)₃ (3.180 g, 15.00 mmol) was dissolved in 25 mL CH₂Cl₂ was added, and the solution allowed to stir overnight under argon. The resulting solution was washed with 1 M NaOH (aq), then saturated NaHCO₃ (aq), and finally deionized water. The organic layer was passed through a plug of activated Al₂O₃ and evaporated in vacuo, resulting in a brown powder (1.336 g, 53.65%). ¹H NMR (400 MHz, CDCl₃) δ 2.487 (br s, 8H, CH₂^A), 3.519 (s, 4H, CH₂^B), 7.313 (m, 10H CHPh). ¹³C{¹H} NMR (100 MHz, CDCl₃): δ 53.288, 63.266, 127.266, 128.398, 129.453.

1,4-bis(pyridin-2-ylmethyl)piperazine (3):

Piperazine (0.811 g, 10.00 mmol) and 2-pyridinecarboxaldehyde (2.144 g, 20.00 mmol) were dissolved in 30 mL of CH₂Cl₂ and stirred under Ar at room temp. To this solution a few drops of trifluoroacetic acid (0.2 mL) were added, and the mixture was allowed to stir for 30 min, producing a clear yellow solution. Next, NaBH(OAc)₃ (3.171 g, 15.00 mmol) dissolved in 25 mL CH₂Cl₂ was added, and the solution allowed to stir overnight under Ar. The resulting solution was washed with 1 M NaOH (aq), then saturated NaHCO₃ (aq), and finally deionized water. The organic layer was placed in the freezer and allowed to crystallize. The crystalline precipitate was collected via filtration (1.174 g, 79.2%). X-ray quality crystals were grown by cooling a 0.15 M solution in CH₂Cl₂ to -5 °C. ¹H NMR (400 MHz, CDCl₃) δ 2.5 (s, 8H, CH₂^A), 3.6 (s, 4H, CH₂^B), 7.08 (t, 1H, J=6.64 Hz, Py^D), 7.33 (d, J=7.8 Hz, 1H, Py^C), 7.56 (t, 1H, J=7.82 Hz, Py^E), 8.47 (s, 1H, Py^F). ¹³C{¹H} NMR (100 MHz, CDCl₃) δ 53.43, 64.79, 122.15, 123.41, 136.48, 149.42, 158.81. Anal. Calcd. for C₁₆H₂₀N₄: C, 71.61; 16.20 4H, 7.51; N, 20.88.¹⁷ Found: C, 71.46; H, 7.67; N, 21.24.¹⁷

1,4-Diphenethylpiperazine (4):

Piperazine (0.431 g, 5.00 mmol) and phenylacetaldehyde (1.204 g, 10.00 mmol) were dissolved in 30 mL of CH₂Cl₂ and stirred under Ar at room temp. To this solution a few drops of trifluoroacetic acid (0.2 mL) were added, and the mixture was allowed to stir for 30 min, producing a clear yellow solution. Next, NaBH(OAc)₃ (2.109 g, 10.00 mmol) dissolved in 25 mL CH₂Cl₂ was added, and the solution allowed to stir overnight under Ar. The resulting solution was washed with 1 M NaOH (aq), then saturated NaHCO₃ (aq), and finally deionized water. The organic layer was placed in the freezer and allowed to crystallize. The crystalline precipitate was collected via filtration (1.174 g, 79.2%). X-ray quality crystals were grown by cooling a 0.15 M solution in CH₂Cl₂ to -5 °C. ¹H NMR (400 MHz, CDCl₃) δ 2.62 (m, 12H, CH₂^A, CH₂^B), 2.81 (dd, J=11.7, 7.7 Hz, 4H, CH₂^C), 7.20 (m, 6H, Ph^{o,p}), 7.27 (t, J=7.4 Hz, 4H, Ph^m). ¹³C{¹H} NMR (100 MHz,

CDCl_3) δ 33.82, 53.38, 60.73, 126.28, 128.62, 128.92, and 140.53. Anal. Calcd. for $\text{C}_{20}\text{H}_{26}\text{N}_2$: C, 81.59; H, 8.89; N, 9.52. Found: C, 81.12; H, 8.73; N, 8.74.

1-Benzhydryl-4-benzylpiperazine (5):

Diphenylmethylpiperazine (3.061 g, 12.00 mmol) and benzaldehyde (1.281 g, 12.00 mmol) were dissolved in 30 mL CH_2Cl_2 and stirred under Ar at room temp. To this solution a few drops of trifluoroacetic acid (0.2 mL) were added, and the mixture was allowed to stir for 30 min, producing a clear solution. Next, $\text{NaBH}(\text{OAc})_3$ (2.539 g, 12.00 mmol) dissolved in 25 mL CH_2Cl_2 was added, and the mixture was allowed to stir overnight under Ar. The resulting solution was washed with 1 M NaOH (aq), then saturated NaHCO_3 (aq), and finally deionized water. The organic layer was passed through a plug of activated Al_2O_3 and evaporated *in vacuo*, resulting in a white powder that was dried overnight under vacuum (1.340 g, 59.29%). X-ray quality crystals were obtained through slow evaporation of a pentane solution. ^1H NMR (400 MHz, CDCl_3) δ 2.46 (m, 8H, CH_2^{A} , CH_2^{B}), 3.51 (s, 2H, CH_2^{C}), 4.22 (s, 1H, CH), 7.15 (t, $J = 7.0$ Hz, 2H, CHPh_2^{P}), 7.25 (m, 9H, Ph), 7.39 (d, $J = 7.0$ Hz, 4H, CHPh_2^{O}). $^{13}\text{C}\{^1\text{H}\}$ NMR (100 MHz, CDCl_3) δ 52.14, 53.59, 65.30, 76.44, 127.06, 127.18, 128.21, 128.36, 128.62, 129.45, 138.37, 143.04. Anal. Calcd. for $\text{C}_{24}\text{H}_{26}\text{N}_2$: C, 84.17; H, 7.65; N, 8.18. Found: C, 83.89; H, 7.53; N, 7.96.

1-Benzhydryl-4-(pyridin-2-ylmethyl)piperazine (6):

Diphenylmethylpiperazine (2.526 g, 10.00 mmol) and 2-pyridinecarboxaldehyde (1.070 g, 10.00 mmol) were dissolved in 30 mL CH_2Cl_2 and stirred under Ar at room temp. To this solution a few drops of trifluoroacetic acid (0.2 mL) were added and the mixture was allowed to stir for 30 min, producing a clear yellow solution. Next, $\text{NaBH}(\text{OAc})_3$ (2.158 g, 10.00 mmol) dissolved in 25 mL CH_2Cl_2 was added, and the mixture was allowed to stir overnight under Ar. The resulting solution

was washed with 1 M NaOH (aq), then saturated NaHCO₃ (aq), and finally deionized water. The organic layer was passed through a plug of activated Al₂O₃ and evaporated *in vacuo*. The resulting thick yellow oil solidified into a beige powder under vacuum (1.34 g, 59.3%). X-ray quality crystals were obtained by layering a 20 mM solution in CH₃CN with ether in a 5 mm diameter tube. ¹H NMR (400 MHz, CDCl₃) δ 2.44 (br s, 4H, CH₂^A), 2.54 (br s, 4H, CH₂^B), 3.66 (s, 2H, CH₂^C), 4.23 (s, 1H, CH), 7.15 (m, 3H, Ph^p, Py^F), 7.25 (t, J=7.8 Hz, 4H, Ph^m), 7.37 (d, J= 7.8, 1H, Py^D), 7.40 (d, J=6.3 Hz, 4H, Ph^o), 7.61 (td, J=7.8, 1.6 Hz, 1H, Py^F), 8.54 (d, J = 5.1 Hz, 1H, Py^G). ¹³C{¹H} NMR (100 MHz, CDCl₃) δ 51.81, 53.57, 64.57, 76.17, 121.88, 123.13, 126.82, 127.94, 128.38, 136.21, 142.75, 149.21, 158.64. Anal. Calcd. for C₂₃H₂₅N₃: C, 80.43; H, 7.33; N, 12.24. Found: C, 79.81; H, 7.30; N, 11.90.

(CuI)₂(N,N'-Dibenzylpiperazine), (CuI)₂(2):

The compound was prepared in analogous fashion to (CuI)₂(**8**), using 5.00 mmol **2** and 10.0 mmol CuI, yielding 2.326 g product (3.593 mmol, 71.9%). Anal. Calcd for C₁₈H₂₂N₂Cu₂I₂: C, 33.40; H, 3.43; N, 4.33. Found: C, 33.33; H, 3.39; N, 4.40. TGA Calcd for CuI: 58.8. Found: 59.6 (150–190 °C).

(CuI)₂(N,N'-(bis-2-Pyridylmethyl)piperazine), (CuI)₂(3):

The compound was prepared in analogous fashion to (CuI)₂(**8**), using 2.09 mmol **3** and 4.00 mmol CuI, yielding 0.640 g product (0.986 mmol, 49.3%). Anal. Calcd for C₁₆H₂₀N₄Cu₂I₂: C, 29.60; H, 3.10; N, 8.63. Found: C, 30.24; H, 3.17; N, 8.65. TGA Calcd for CuI: 58.7. Found: 56.8 (160–210 °C).

(CuI)₂(N,N'-bis-Phenethylpiperazine), (CuI)₂(4):

The compound was prepared in analogous fashion to $(\text{CuI})_2(\mathbf{8})$, using 3.81 mmol **4** and 7.57 mmol CuI, yielding 1.295 g product (1.918 mmol, 50.3%). Anal. Calcd for $\text{C}_{20}\text{H}_{26}\text{N}_2\text{Cu}_2\text{I}_2$: C, 35.57; H, 3.88; N, 4.15. Found: C, 35.61; H, 3.88; N, 4.14. TGA Calcd for CuI: 56.4. Found: 57.1 (160–210 °C).

$(\text{CuI})_2(1\text{-benzhydryl-4-(pyridin-2-ylmethyl)piperazine})_2, (\text{CuI})_2(\mathbf{6})_2$:

The compound was prepared in analogous fashion to $(\text{CuI})_2(\mathbf{8})$, using 3.43 mmol **6** and 10.0 mmol CuI, yielding 0.998 g product (0.935 mmol, 54.5%). Anal. Calcd for $\text{C}_{23}\text{H}_{25}\text{N}_3\text{Cu}_2\text{I}_2$: C, 51.74; H, 4.72; N, 7.87. Found: C, 51.79; H, 4.68; N, 7.86. TGA Calcd for CuI: 52.6. Found: 55.8 (260–290 °C).

$(\text{CuI})_2(\text{N,N'-Diethylpiperazine}), (\text{CuI})_2(\mathbf{8})$:

N,N'-Diethylpiperazine (**8**, 5.00 mmol) was dissolved in 25 mL of MeCN. CuI (10.0 mmol) was dissolved in a separate 50 mL portion of MeCN under Ar. The solution of **8** was added to the CuI solution via syringe. A white precipitate formed within seconds of addition. The suspension was refluxed for 3 h to ensure complete reaction. The white precipitate was collected via filtration, washed with MeCN and ethyl ether, and dried under vacuum (1.619 g, 3.095 mmol, 61.9%). Anal. Calcd for $\text{C}_8\text{H}_{18}\text{N}_2\text{Cu}_2\text{I}_2$: C, 18.37; H, 3.47; N, 5.35. Found: C, 18.34; H, 3.37; N, 5.32. TGA Calcd for CuI: 72.8. Found: 73.4 (115–135 °C).

$(\text{CuI})_4(\text{N-Diphenylmethylpiperazine})_4, (\text{CuI})_4(\mathbf{10})_4$:

The compound was prepared in analogous fashion to $(\text{CuI})_2(\mathbf{8})$, using 5.00 mmol **10** and 5.00 mmol CuI, yielding 0.984 g product (0.556 mmol, 44.5%). Anal. Calcd for $\text{C}_{68}\text{H}_{80}\text{N}_8\text{Cu}_4\text{I}_4$: C, 46.11;

H, 4.55; N, 6.33. Found: C, 46.71; H, 4.54; N, 6.44. TGA Calcd for $(\text{CuI})_5(\mathbf{10})_4$: 88.6. Found 88.6
(185–205 °C). Calcd for CuI: 43.0. Found: 43.5 (205–245 °C).

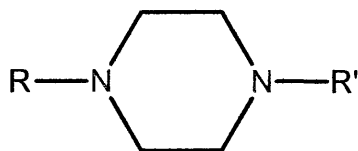
RESULTS AND DISCUSSION

Copper(I) materials have been of significant interest to the Pike research group for their ability to interact with VOCs in a labile manner, producing luminescent adducts. In this work we strove to develop a viable luminescent detector for various volatile amines and sulfides using CuI. This was pursued through the generation of unsaturated 3-coordinate Cu(I) centers constrained by steric interactions of the coordinated ligands. A series of chemical synthesis and fabrication methods were used to make these detector materials: reductive amination to form the ligands, simple self-assembly under reflux to produce copper(I) iodide complexes with the ligands, and vapor exposure and spectroscopy to test the luminescent response of the various complexes.

Ligand Generation.

Previous work in our lab has shown that varying ligand size, shape, and binding characteristics can have a significant impact on the type of network CuI will form and its chemical properties. Piperazine was chosen for the ease with which one can manipulate the substituents at the N and N' positions (**Scheme 2**) while also retaining access to the nitrogen lone pair for metal complexation.

Scheme 2

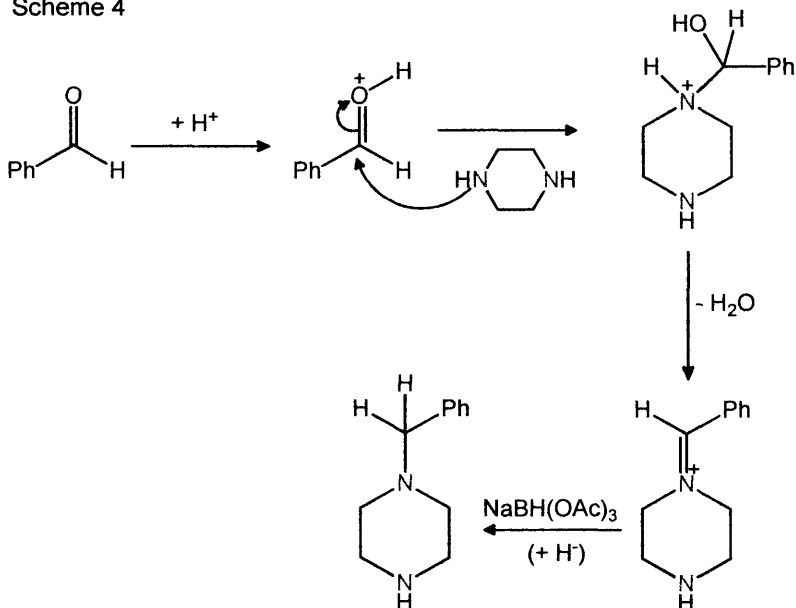


- | | |
|--|---|
| 1: R = CH ₂ CH ₃ , R' = CHPh | 6: R = CH ₂ -2-pyridyl, R' = CHPh ₂ |
| 2: R,R' = CH ₂ Ph | 7: R, R' = CH ₃ |
| 3: R,R' = CH ₂ -2-pyridyl | 8: R, R' = CH ₂ CH ₃ |
| 4: R,R' = CH ₂ CH ₂ Ph | 9: R, R' = Ph |
| 5: R = CH ₂ Ph, R' = CHPh ₂ | 10: R = H, R' = CHPh ₂ |

Compounds **1-6** were prepared through reductive amination by stirring piperazine and aldehyde overnight in the presence of reducing agent, as indicated in **Schemes 3** and **4**, whereas compounds **7-10** were purchased. As suggested by **Scheme 4**, the aldehyde is first protonated in order to generate an electron deficient carbonyl carbon. This process was aided by the addition of TFA to promote protonation. Next, piperazine acts as a nucleophile and attacks the carbonyl carbon, generating the intermediate shown. The observed OH groups are also protonated and dehydration is observed. This highly electrophilic carbon then pulls electron density from the adjacent N and forms the incipient iminium ion intermediate. Finally, triacetoxyborohydride anion reduces the iminium ion to the desired 1,4-dibenzylpiperazine. Similarly, all the ligands synthesized herein were prepared roughly following this mechanism with minor alterations. For example, species **1** was generated by reacting 1-ethylpiperazine with one equivalent of benzaldehyde. For the homo-disubstituted **4**, piperazine was reacted with two equivalents of phenylacetaldehyde; similar methods were used in the formation of compounds **2** and **3**. The hetero-disubstituted **5** and **6** were prepared by reacting N-diphenylmethylpiperazine with benzaldehyde and 2-pyridinecarboxaldehyde, respectively. The reactions produced beige to brown solids that precipitated upon cooling or evaporation. The

analytically pure compounds were then crystallized for X-ray diffraction. Since its structure was as yet unreported, commercial 1,4-diphenylpiperazine (**8**) was also crystallized for X-ray diffraction.

Scheme 4



Crystallographic data were acquired for compounds **2-6** and **9**; however, the structures of only ligands **4**, **5**, **6**, and **9** were found to be novel, **Figure 11**. Species **1** and **7** were not studied crystallographically because they are oils under ambient conditions. Crystallographic determination information is given in **Table 2** and selected bond lengths and angles in **Table 3**. Compound **4** crystallized in the monoclinic space group $C2/c$, being half independent due to the presence of an inversion center at the center of the piperazine ring. Compound **9** crystallized in the orthorhombic space group $Pbca$. As was the case with **4**, an inversion center at the ring centroid of **9** resulted in a half independent molecule. Compound **6** was found to crystallize in the monoclinic space group $P2/c$ with a fully independent molecular unit. Compound **5**

Compound **4** crystallized in the monoclinic space group *C2/c*, being half independent due to the presence of an inversion center at the center of the piperazine ring. Compound **9** crystallized in the orthorhombic space group *Pbca*. As was the case with **4**, an inversion center at the ring centroid of **9** resulted in a half independent molecule. Compound **6** was found to crystallize in the monoclinic space group *P2/c* with a fully independent molecular unit. Compound **5** crystallized in the non centrosymmetric monoclinic space group *Pn*, and was found to be fully independent.

Table 2. Disubstituted piperazine crystal and structure refinement data.

	1,4-dibenzylpiperazine ^b (2)	1,4-bis(pyridin-2-ylmethyl)piperazine ^c (3)	1,4-Diphenethylpiperazine (4)
CCDC deposit no.	746715 ^b	104615	863658
color and habit	Colorless block	Colorless prism	Colorless prism
size, mm	0.25 x 0.13 x 0.11	1.2 x 0.9 x 0.2	0.07 x 0.12 x 0.32
formula	C ₁₈ H ₂₂ N ₂	C ₁₆ H ₂₀ N ₄	C ₂₀ H ₂₆ N ₂
formula weight	266.38	268.34	296.46
space group	<i>Pbca</i>	<i>P21/c</i>	<i>C2/c</i>
<i>a</i> , Å	7.42450(10)	5.736(2)	17.9064(13)
<i>b</i> , Å	18.8323(2)	7.369(2)	6.2517(5)
<i>c</i> , Å	21.1707(3)	17.274(5)	14.9869(11)
α , deg	90	90	90
β , deg	90	99.06(2)	90.613(4)
γ , deg	90	90	90
volume, Å ³	2960.10(7)	721.0(4)	1677.6(2)
Z	8	2	4
ρ_{calc} , g cm ⁻³	1.195	1.236	1.174
F ₀₀₀	1152	288	648
μ (Cu K α), mm ⁻¹	0.535	0.6	0.516
radiation	CuK α (λ = 1.54178 Å)	CuK α	CuK α (λ = 1.54178 Å)
temperature, K	100	100	100
residuals: ^a R; R _w	0.0350, 0.0967	0.059, 0.060	0.0374, 0.0943
goodness of fit	1.007		1.075

^a) $R = R_1 = \sum ||F_o| - |F_c|| / \sum |F_o|$ for observed data only. ^b) CCDC 746715. ¹⁶ ^c) CCDC 104615. ¹⁷
 $R_w = wR_2 = \{\sum [w(F_o^2 - F_c^2)^2] / \sum [w(F_o^2)^2]\}^{1/2}$ for all data.

Table 2. (continued)	1-Benzhydryl-4-benzylpiperazine (5)	1-Benzhydryl-4-(pyridin-2-ylmethyl)-piperazine (6)	1,4-Diphenylpiperazine (9)
CCDC deposit no.	863660	863661	863662
color and habit	Colorless plate	Colorless plate	Colorless plate
size, mm	0.44 × 0.16 × 0.06	0.44 × 0.19 × 0.07	0.28 × 0.27 × 0.14
formula	C ₂₄ H ₂₆ N ₂	C ₂₃ H ₂₅ N ₃	C ₁₆ H ₂ N ₁₈
formula weight	342.48	343.47	238.67
space group	<i>Pn</i>	<i>P2/c</i>	<i>Pbca</i>
<i>a</i> , Å	5.9450(2)	13.5637(2)	8.6980(7)
<i>b</i> , Å	19.0722(4)	5.82170(10)	8.4287(7)
<i>c</i> , Å	8.6084(2)	24.0645(4)	17.6359(15)
α, deg	90	90	90
β, deg	98.1790(10)	96.4600(10)	90
γ, deg	90	90	90
volume, Å ³	966.13(4)	1888.16(5)	1292.94(19)
Z	2	4	4
ρ _{calc} , g cm ⁻³	1.177	1.208	1.224
F ₀₀₀	368	736	512
μ(Cu Kα), mm ⁻¹	0.522	0.551	0.556
radiation	CuKα (λ= 1.54178 Å)	CuKα (λ= 1.54178 Å)	CuKα (λ= 1.54178 Å)
temperature, K	100	100	100
residuals: ^a R; R _w	0.0279, 0.0684	0.0312, 0.0801	0.0353, 0.0906
goodness of fit	1.055	1.044	1.071

^a) $R = R_1 = \sum ||F_o| - |F_c|| / \sum |F_o|$ for observed data only. ^b) CCDC 746715. ¹⁶ ^c) CCDC 104615. ¹⁷ $R_w = wR_2 = \{\sum [w(F_o^2 - F_c^2)^2] / \sum [w(F_o^2)^2]\}^{1/2}$ for all data.

Table 3. Disubstituted piperazines selected bond lengths and angles.

1,4-dibenzylpiperazine (2)			
N(1)-C(5)	1.4562(13)	C(5)-N(1)-C(1)	112.18(8)
N(1)-C(1)	1.4628(14)	C(5)-N(1)-C(4)	112.50(8)
N(1)-C(4)	1.4622(13)	C(1)-N(1)-C(4)	109.20(8)
N(2)-C(12)	1.4582(14)	C(12)-N(2)-C(3)	111.81(8)
N(2)-C(3)	1.4645(14)	C(12)-N(2)-C(2)	110.68(8)
N(2)-C(2)	1.4643(13)	C(3)-N(2)-C(2)	109.04(8)
C(1)-C(2)	1.5144(15)	N(1)-C(1)-C(2)	109.66(8)
C(3)-C(4)	1.5201(15)	N(2)-C(2)-C(1)	110.07(8)
		N(1)-C(4)-C(3)	109.64(8)

		N(2)-C(3)-C(4)	110.38(8)
1,4-bis(pyridin-2-ylmethyl)piperazine (3)¹⁷			
N(2)-C(7)	1.459(2)	C(7)-N(8)-C(9)	111.99(14)
N(2)-C(8)	1.460(2)	C(7)-N(8)-C(10)	111.94(14)
N(2)-C(6)	1.456(2)	C(9)-N(8)-C(10)	109.16(14)
1,4-Diphenethylpiperazine (4)			
N-C(1)	1.4589(17)	C(1)-N-C(2)	108.67(10)
N-C(2)	1.4617(16)	C(1)-N-C(3)	110.58(10)
N-C(3)	1.4611(16)	C(2)-N-C(3)	112.14(10)
1-Benzhydryl-4-benzylpiperazine (5)			
N(1)-C(8)	1.459(2)	C(8)-N(1)-C(10)	108.61(11)
N(1)-C(10)	1.4600(18)	C(8)-N(1)-C(7)	111.86(12)
N(1)-C(7)	1.463(2)	C(10)-N(1)-C(7)	110.26(12)
N(2)-C(11)	1.4686(18)	C(11)-N(2)-C(9)	107.92(11)
N(2)-C(9)	1.4690(19)	C(11)-N(2)-C(12)	110.04(12)
N(2)-C(12)	1.477(2)	C(9)-N(2)-C(12)	110.60(11)
C(10)-C(11)	1.514(2)	N(1)-C(8)-C(9)	110.67(12)
C(8)-C(9)	1.518(2)	N(2)-C(9)-C(8)	111.23(12)
		N(1)-C(10)-C(11)	110.27(12)
		N(2)-C(11)-C(10)	110.73(13)
1-Benzhydryl-4-(pyridin-2-ylmethyl)piperazine (6)			
N(1)-C(4)	1.4583(14)	C(4)-N(1)-C(1)	108.69(8)
N(1)-C(1)	1.4585(13)	C(4)-N(1)-C(18)	111.64(8)
N(1)-C(18)	1.4600(13)	C(1)-N(1)-C(18)	111.32(8)
N(2)-C(3)	1.4678(13)	C(3)-N(2)-C(2)	108.83(8)
N(2)-C(2)	1.4699(13)	C(3)-N(2)-C(5)	108.81(8)
N(2)-C(5)	1.4807(13)	C(2)-N(2)-C(5)	110.93(8)
C(3)-C(4)	1.5161(15)	N(1)-C(1)-C(2)	110.20(9)
C(1)-C(2)	1.5153(15)	N(2)-C(2)-C(1)	110.47(9)
		N(2)-C(3)-C(4)	111.99(9)
		N(1)-C(4)-C(3)	109.82(9)
1,4-diphenylpiperazine (9)			
N(1)-C(1)	1.4589(15)	C(3)-N(1)-C(1)	116.84(9)
N(1)-C(2)	1.4695(15)	C(3)-N(1)-C(2)	115.48(9)
N(1)-C(3)	1.4157(15)	C(1)-N(1)-C(2)	110.18(9)

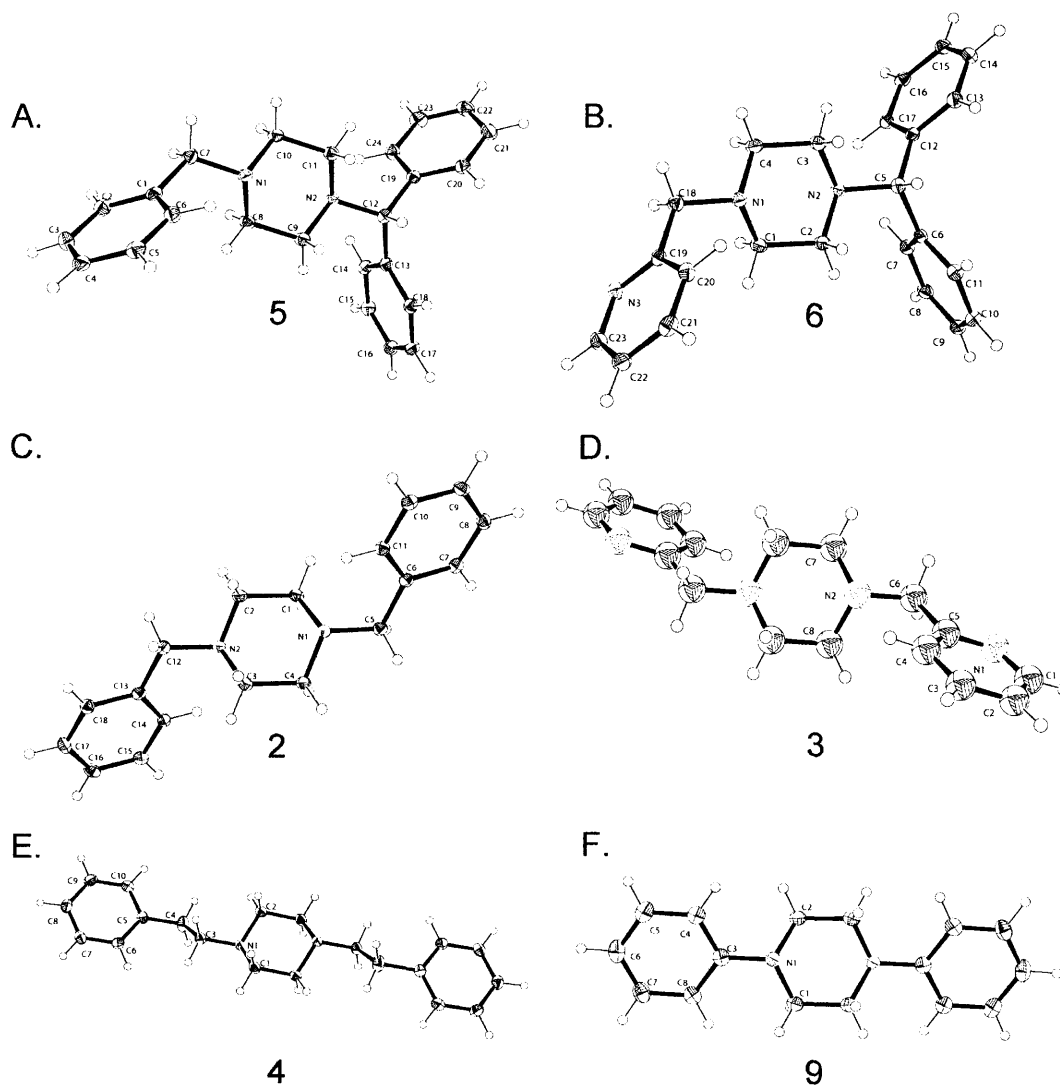


Figure 11. Thermal ellipsoid drawings of **5** (A), **6** (B), **2** (C), **3** (D),¹⁷ **4** (E), and **9** (F).

Numerous related N,N'-disubstituted piperazines have previously been reported, including ring-substituted N,N'-diphenylpiperazines (**10**),¹⁸ piperazines with the N-CHPh₂ substituent,¹⁹ the simple N,N'-dibenzylpiperazine (**2**),²⁰ and 1,4-bis(pyridin-2-ylmethyl)piperazine (**3**).^{17,21} Compounds **2-6** and **9** are overlaid for structural comparison in **Figure 12**. All piperazine carbon-nitrogen and carbon-carbon bond lengths were found to be within the expected range.

Bond angles around the piperazine nitrogen ranged between 107.9–112.5° depending upon the substituents attached to the piperazine ring, as shown in **Figure 12** and **Table 2**. The phenyl groups in compound **9** appear to force more planar orientations and flatter bond angles about the nitrogen atoms, approaching the 120° value associated with sp^2 hybridized nitrogen. This effect may be attributed to the delocalization of the nitrogen lone pair caused by the electron-withdrawing aromatic system directly bonded to the nitrogen, as shown in **Scheme 5**. By way of contrast, in structures **2-6** the aromatic substituents are all at least one carbon removed from the piperazine ring, allowing for a more tetrahedral conformation and angles much closer to the canonical sp^3 hybridized value of 109.5°.

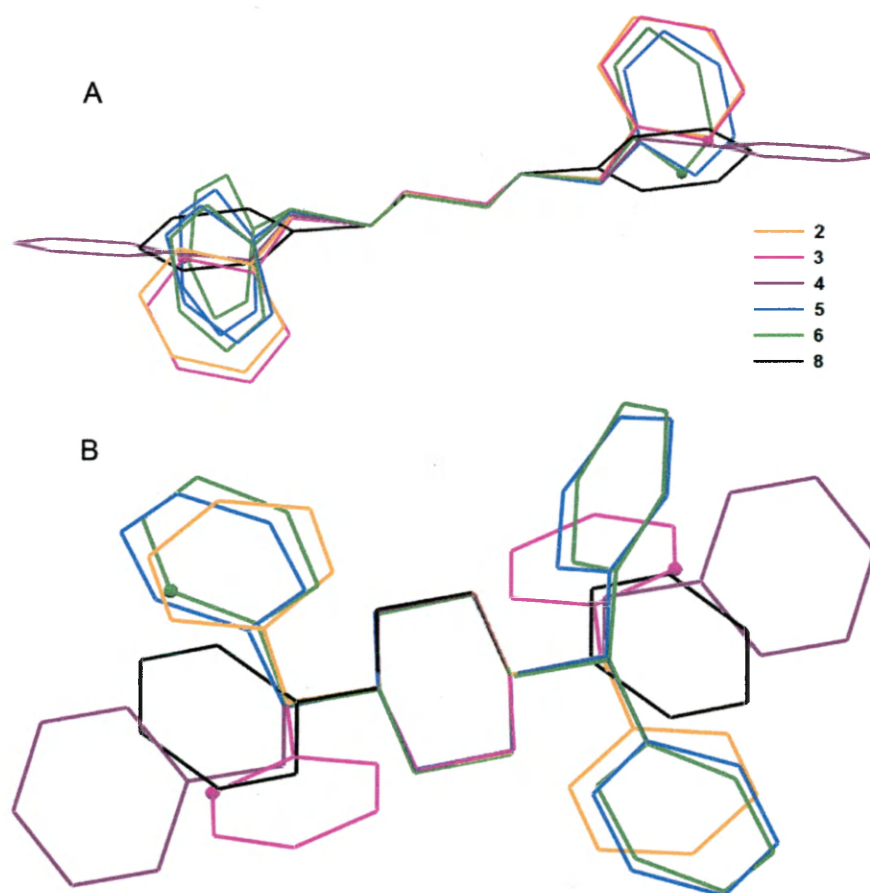
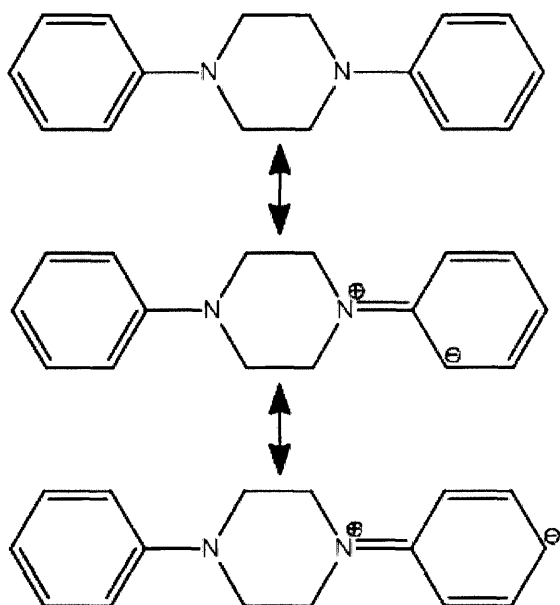


Figure 12. Disubstituted piperazine overlay of substituent orientation. A: Compounds **2-6** and **9** overlaid using the piperazine rings. B: N/N' groups, ring nitrogen atoms are shown as spheres.

Scheme 5



Multiple short, non-bonded intermolecular interactions were observed in all four structures. Compound **9** showed close intermolecular interactions between H1B and C7 (2.880(14) Å), H2B and C5 (2.826(14) Å), H4 and C6 (2.862(14) Å) and H6 and C4 (2.768(16) Å). Compound **4** demonstrated intermolecular interactions between H6 and a phenyl ring centroid C5–C10 (2.70(3) Å) and between H3A and C7 (2.887(14) Å). Compound **5** revealed a variety of intermolecular interactions: between H9B and C4 (2.687(18) Å), ring centroid C13–C18 and H4 (2.82(3) Å), and bond centroid C4/C5 and H7B (2.74(3) Å). Finally, some of the closest intermolecular interactions were seen in compound **6** between the pyridyl nitrogen N3 and phenyl H9 and H21 with distances of (2.557(14) Å) and (2.734(14) Å). Further intermolecular interactions were seen between H1A and C8, (2.883(13) Å), and finally between H22 and phenyl centroid C6–C11, (2.61(2) Å). In all compounds, these non-bonded interactions weakly knit the structures into three dimensional networks, **Figure 13**.

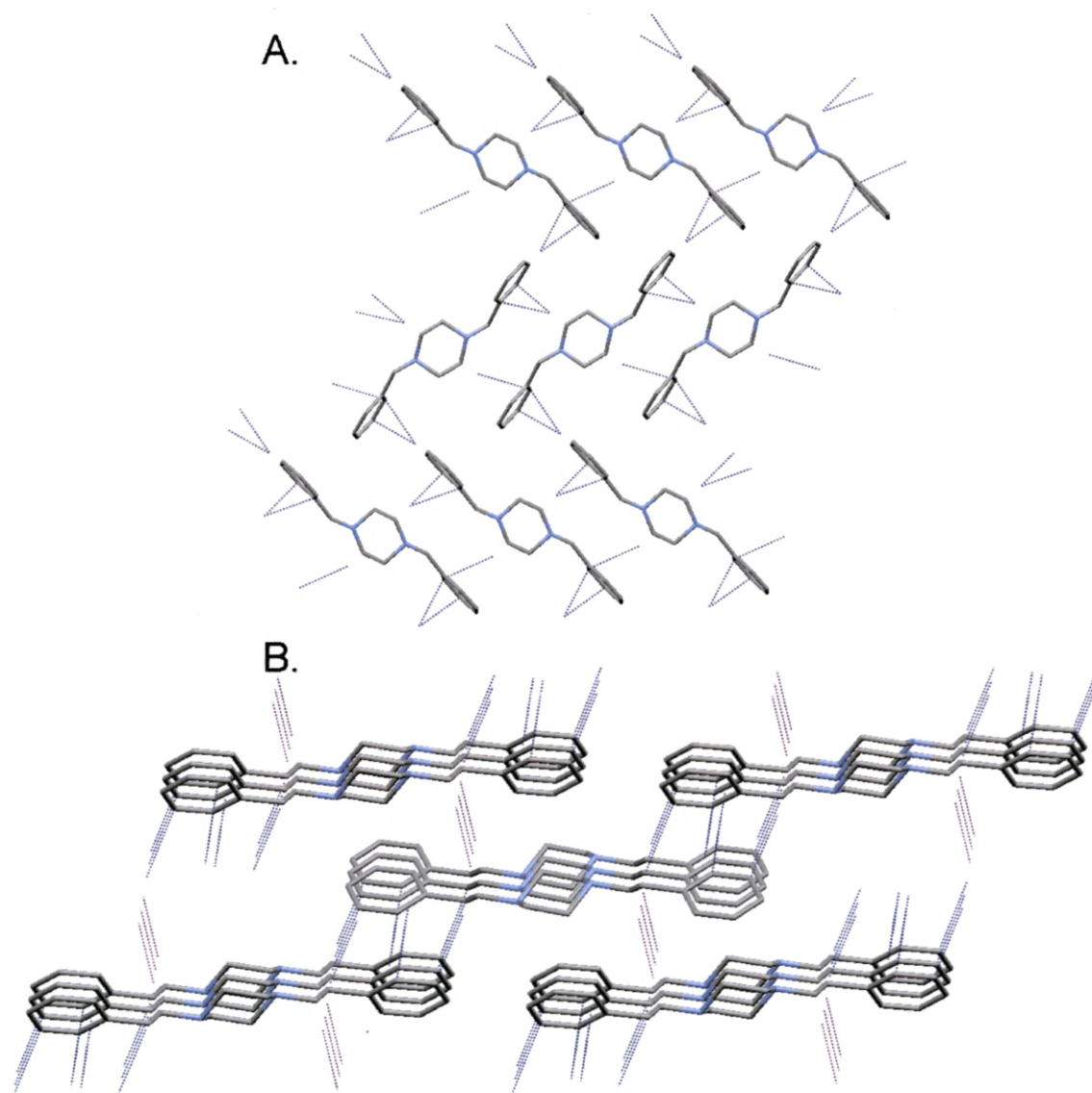


Figure 13. Short contact interaction for ligand species **2** (A) and **4** (B) shown as dotted lines between molecules.

CuI Complex Synthesis.

The N,N'-disubstituted piperazines **1–10** were each individually dissolved in acetonitrile and then combined in stoichiometric amounts of CuI, which was also dissolved in acetonitrile. Addition of ligands **2, 3, 4, 6, 8,** and **10** immediately produced solid products, while addition of ligands **1, 5,** and **9** yielded no reaction and returned starting material. The suspensions were

refluxed for a minimum of three hours to ensure complete reaction and a uniform product. The isolatable products were then removed from the mother liquor and found to be very stable in air, with no evident decomposition even after several months of storage. Furthermore, the products were white (**2**, **4**, **8**, and **10**) or yellow (**3** and **6**) microcrystalline powders, the yellow color being associated with the ligands bearing a 2-methylpyridine group. Once the various complexes were generated, TGA, combustion elemental analysis, and X-ray crystallography were used to confirm the metal to ligand ratio and chemical structure in all cases. The TGA analyses resulted in smooth ligand loss yielding CuI in virtually all cases (see Thermogravimetric Analysis Section below). Single crystals for all compounds were formed from unstirred solventothermal reaction mixtures in acetonitrile at 100 °C or layered CuI and ligand solutions in narrow tubes at 25 °C. In all cases, the results of all three analysis procedures revealed identical metal to ligand ratios.

X-ray Crystallography and CuI Complex Trends.

The intent behind manipulating the substituents of the N,N'-piperazine ligands was to force the formation of 3-coordinate copper(I) centers by means of steric control in order to avoid the commonly encountered 4-coordinate structures, such as cubanes (CuI)₄L₄ or square dimers, (CuI)₂L₄ (see **Scheme 1**). Instead, the aim here was to produce 3-coordinate polymeric chains similar to network displayed in **Figure 8**. Although this arrangement is not often observed, it has been reported in the CuI complex of phenazine, **Figure 14**.²²

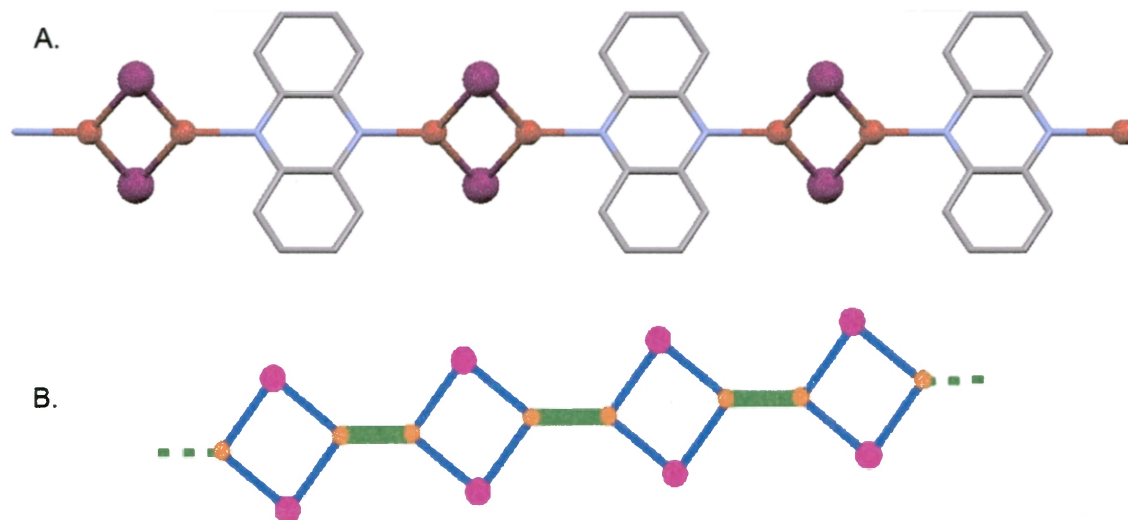


Figure 14. A) 3-coordinate (CuI)₂(Phenazine) complex. B) 3-coordinate framework to be emulated by our substituted piperazines.

X-ray crystal structures were solved for CuI species of ligands **2**, **3**, **4**, **6**, **8**, and **10** and the structural solution data is shown below in **Table 4** and select bond angles are displayed **Table 5**.

Table 4. CuI piperazine complex crystal structure refinement data.

	(CuI) ₂ (2)	(CuI) ₂ (3)	(CuI) ₂ (4)
CCDC dep. no.	877786	877788	877791
color and habit	colorless prism	yellow needle	colorless blade
size, mm	0.42 × 0.14 × 0.10	0.23 × 0.05 × 0.04	0.34 × 0.18 × 0.02
formula	C ₉ H ₁₁ CuIN	C ₁₆ H ₂₀ Cu ₂ I ₂ N ₄	C ₂₀ H ₂₆ Cu ₂ I ₂ N ₂
formula weight	323.63	649.24	675.31
space group	<i>P</i> 2 ₁ / <i>n</i> (#14)	<i>P</i> -1 (#2)	<i>P</i> 2 ₁ / <i>c</i> (#14)
<i>a</i> , Å	7.7387(3)	8.6487(2)	8.4848(3)
<i>b</i> , Å	16.7925(5)	9.9098(2)	20.3374(7)
<i>c</i> , Å	8.2424(3)	12.4157(3)	13.1364(4)
α, deg	90	112.8310(10)	90
β, deg	110.6170(10)	91.449(2)	92.548(2)
γ, deg	90	95.4470(10)	90
volume, Å ³	1002.52(6)	974.07(4)	2264.56(13)
<i>Z</i>	4	2	4
ρ _{calc} , g cm ⁻³	2.144	2.214	1.981
<i>F</i> ₀₀₀	616	616	1296
μ _{Cu Kα} , mm ⁻¹	26.796	27.613	23.758

radiation	CuK α ($\lambda = 1.54178$ Å)	CuK α ($\lambda = 1.54178$ Å)	CuK α ($\lambda = 1.54178$ Å)
temperature, K	100	100	100
residuals: ^a R; R _w	0.0257; 0.0646	0.0306; 0.0762	0.0419; 0.1221
goodness of fit	1.12	1.066	1.022

^aR = $R_1 = \Sigma ||F_o| - |F_c|| / \Sigma |F_o|$ for observed data only. R_w = $wR_2 = \{\Sigma [w(F_o^2 - F_c^2)^2] / \Sigma [w(F_o^2)^2]\}^{1/2}$ for all data.

Table 4. (continued)	(CuI) ₂ (6) ₂	(CuI) ₂ (8)	(CuI) ₄ (10) ₄
CCDC dep. no.	877789	877783	877790
color and habit	yellow prism	colorless plate	colorless plate
size, mm	0.24 × 0.12 × 0.11	0.27 × 0.15 × 0.06	0.15 × 0.12 × 0.05
formula	C ₄₆ H ₅₀ Cu ₂ I ₂ N ₆	C ₄ H ₉ CuIN	C ₆₈ H ₈₀ Cu ₄ I ₄ N ₈
formula weight	1067.8	261.56	1771.16
space group	<i>P</i> 2 ₁ / <i>n</i> (#14)	<i>P</i> 2 ₁ / <i>c</i> (#14)	<i>P</i> -1 (#2)
<i>a</i> , Å	9.6835(3)	7.1527(2)	8.90150(10)
<i>b</i> , Å	22.3183(6)	12.5997(4)	19.1000(3)
<i>c</i> , Å	10.0190(3)	7.8483(3)	21.8081(3)
α , deg	90	90	114.2040(10)
β , deg	93.8350(10)	90.712(2)	92.7600(10)
γ , deg	90	90	90.6140(10)
volume, Å ³	2160.45(11)	707.25(4)	3376.02(8)
Z	2	4	2
ρ_{calc} , g cm ⁻³	1.641	2.456	1.742
F ₀₀₀	1064	488	1744
$\mu_{\text{Cu K}\alpha}$, mm ⁻¹	12.733	37.728	16.127
radiation	CuK α ($\lambda = 1.54178$ Å)	CuK α ($\lambda = 1.54178$ Å)	CuK α ($\lambda = 1.54178$ Å)
temperature, K	100	100	100
residuals: ^a R; R _w	0.0210; 0.0497	0.0287; 0.0732	0.0380; 0.0963
goodness of fit	1.097	1.177	1.011

^aR = $R_1 = \Sigma ||F_o| - |F_c|| / \Sigma |F_o|$ for observed data only. R_w = $wR_2 = \{\Sigma [w(F_o^2 - F_c^2)^2] / \Sigma [w(F_o^2)^2]\}^{1/2}$ for all data.

Table 5. CuI piperazine complex selected bond lengths and angles for all complexes.

(CuI)₂(2)			
Cu-I	2.5507(6), 2.5945(6)	Cu-I-Cu ^a	57.41(2)
Cu-N	2.045(3)	I-Cu-I	122.59(2)
Cu [⋯] Cu	2.4716(11)	I-Cu-N	112.50(9), 124.85(9)
(CuI)₂(3)			
Cu-I	2.5593(6), 2.5729(6), 2.6094(5), 2.6614(6)	Cu-I-Cu ^a	58.873(16), 59.386(17)
Cu-N	2.061(3), 2.073(3), 2.214(3), 2.237(3)	I-Cu-I	122.59(2)
Cu [⋯] Cu	2.5673(7)	I-Cu-N	104.46(8)-120.79(8)
		N-Cu-N	80.25(12), 82.22(12)
(CuI)₂(4)			
Cu-I	2.5245(10), 2.5363(10), 2.5853(10), 2.5711(10)	Cu-I-Cu ^a	58.12(3), 58.16(3)
Cu-N	2.044(5), 2.048(6)	I-Cu-I	121.33(4), 122.38(4)
Cu [⋯] Cu	2.4826(14)	I-Cu-N	111.22(15), 111.74(16), 125.26(16), 127.20(15)
(CuI)₂(6)₂			
Cu-I	2.5428(3), 2.6627(4)	Cu-I-Cu ^a	61.102(13)
Cu-N	2.065(2), 2.2302(18)	I-Cu-I	118.898(13)
Cu [⋯] Cu	2.6479(7)	I-Cu-N	100.07(5), 104.50(5), 121.94(5), 123.67(5)
		N-Cu-N	79.93(7)
(CuI)₄(7)₂			
Cu-I	2.6732(9)-2.7195(9)	Cu-I-Cu ^a	58.93(3)-67.31(3)
Cu-N	2.141(5)-2.148(5)	I-Cu-I	100.48(3)-119.92(3)
Cu [⋯] Cu	2.6686(12)- 2.9377(13)	I-Cu-N	99.47(13)-124.41(15)
(CuI)₂(8)			
Cu-I	2.5431(7), 2.5859(8)	Cu-I-Cu ^a	57.92(3)
Cu-N	2.042(4)	I-Cu-I	122.08(3)
Cu [⋯] Cu	2.4837(14)	I-Cu-N	111.59(11), 126.33(11)
(CuI)₄(10)₄			
Cu-I	2.6090(7)-2.7832(8)	Cu-I-Cu ^a	56.23(2)-60.99(2)
Cu-N	2.052(4)-2.078(4)	I-Cu-I	109.64(2)-117.02(3)
Cu [⋯] Cu	2.6145(10)-2.7045(9)	I-Cu-N	92.40(12)-113.68(11)

^aWithin cluster. ^bNot within cluster.

The desired polymeric structure (**Figure 14**) was only identified for CuI complexes with ligands **2**, **4**, and **8** present. Interestingly, all three of these ligands were symmetric about the piperazine framework, having ethyl, benzyl, or phenethyl substituents in the N and N' positions. The solved structures of (CuI)₂(**2**), (CuI)₂(**4**), and (CuI)₂(**8**) revealed a series of Cu₂I₂ rhomboids (rhombs) linked to the piperazine chair formation at the N and N' positions, forming the observed zigzag and square wave chains in **Figure 15**. Furthermore, the acute angles around the iodide atoms produced sub van der Waals Cu⁺...Cu interactions of 2.4716(11), 2.4826(14) Å, and 2.4837(14) for (CuI)₂(**2**), (CuI)₂(**4**), and (CuI)₂(**8**), respectively (**Table 4**). The copper centers coordinate axially with the piperazine ligands in all cases.

The crystal structures of (CuI)₂(**2**) and (CuI)₂(**8**) showed the independent unit cells to consist of CuI and half of the ligand divided along a mirror plane across the center of the piperazine ring. This creates the zigzag polymer chains shown in **Figure 15**. Conversely, the (CuI)₂(**4**) complex possesses a unit cell in which there are two independent CuI units and two half independent ligands, forming a square wave pattern containing two Cu₂I₂ rhomb orientations and two ligand orientations, **Figure 15**. Additionally, a second C-centered monoclinic polymorph of (CuI)₂(**4**) was observed. The polymorph was crystallized by refrigerating the purified product for several days in dichloromethane, where upon thin plate crystals had formed at the bottom of the solution. This polymorph exhibited the zigzag pattern seen for (CuI)₂(**2**), (CuI)₂(**7**), and the same unit cell pattern of a single CuI unit bound to a half independent ligand molecule divided along the piperazine mirror plane. Unfortunately, a high quality solution for this polymorph proved to be too illusive. In all three structures and the poor quality solution for (CuI)₂(**4**), the ligand substituents on adjacent polymer chains fit together zipper-style, forcing the Cu₂I₂ units on neighboring chains far apart and preventing further

copper iodide bond formation. The closest observed inter-chain Cu^{I} and $\text{Cu}^{\text{II}}\text{Cu}$ approach distances were about 8.1 and 8.7 Å, 5.9 and 7.5 Å, and 6.0 and 6.5 Å for $(\text{CuI})_2(\mathbf{2})$, $(\text{CuI})_2(\mathbf{4})$, and $(\text{CuI})_2(\mathbf{8})$, respectively. Finally, the $(\text{CuI})_2(\mathbf{2})$ complex also had an interesting structural characteristic not seen in the other two species, insofar as it showed a remarkably close intra-chain interaction between an *ortho*-phenyl carbon and copper: $\text{C6}^{\text{II}}\text{Cu1} = 3.016$ Å.

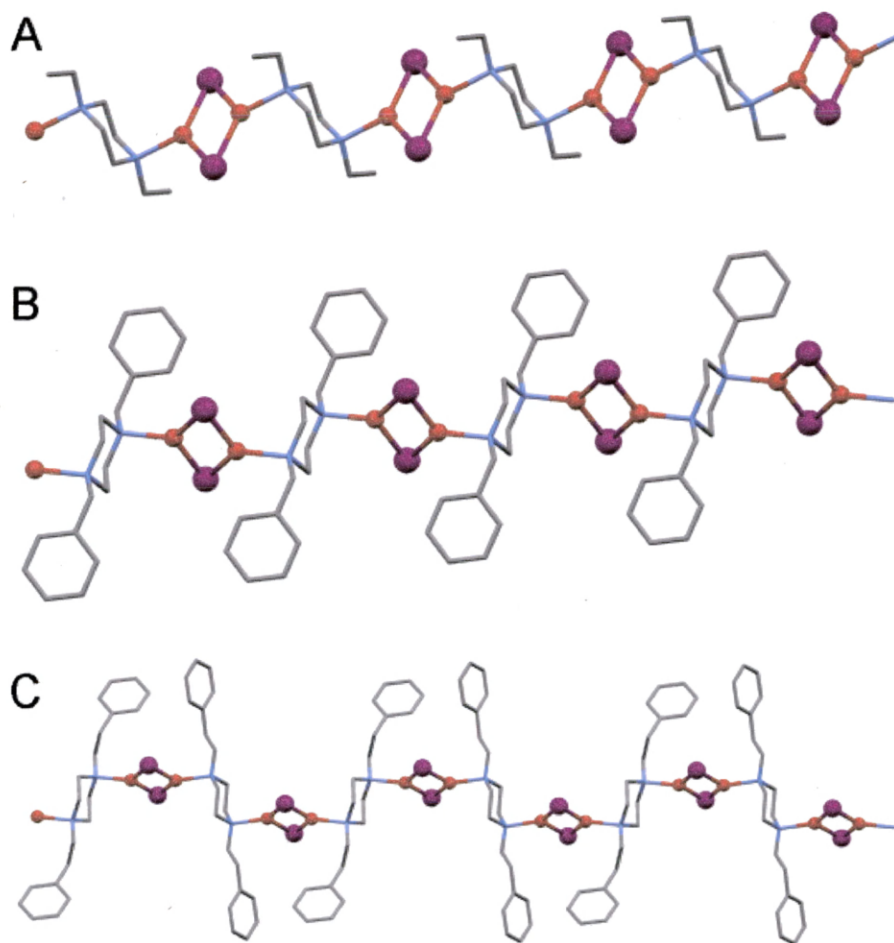


Figure. 15. X-ray structures: **A**, $(\text{CuI})_2(\mathbf{3})$, **B**, $(\text{CuI})_2(\mathbf{4})$, **C**, $(\text{CuI})_2(\mathbf{5})$. X-ray drawing key: H atoms omitted for clarity, ligands shown as wireframe, Cu orange, I violet, N blue, C grey.

The smaller but similarly constructed dimethylpiperazine ligand (**7**) allowed for the formation of a CuI cubane 3-dimensional network typified by triply-bridging μ_3 -I linker. The high

symmetry of **7** and its relatively small methyl substituents allowed the CuI clusters sufficiently close approach to allow formation of Cu_4I_4 cubane units, giving rise to the observed $(\text{CuI})_4(\mathbf{7})_2$, a type **E** network, see **Scheme 1** and **Figure 16**. In this compound, all the bond lengths and angles were similar to the known values from previously reported cubane complexes and networks, while also exhibiting the expected short $\text{Cu}\cdots\text{Cu}$ interactions (2.6234(5)–2.9919(12) Å).⁶⁻⁷ The N,N'-dimethylpiperazine (**7**) ligands were all bonded to the copper atoms in the axial position, as was seen in complexes $(\text{CuI})_2(\mathbf{2})$, $(\text{CuI})_2(\mathbf{4})$, and $(\text{CuI})_2(\mathbf{8})$. By linking together cubane clusters, $(\text{CuI})_4(\mathbf{7})_2$ produces a macrocyclic system identified by a $(\text{Cu}_4\text{I}_4)_6(\mathbf{7})_6$ ring which forms a honeycomb network visible along the *b*-axis, *c*-axis, and diagonally between the *a/b*-axes, **Figure 16**.²³ Related three dimensional networks have also been reported for both CuI DABCO and CuI piperazine systems.^{7,8,9}

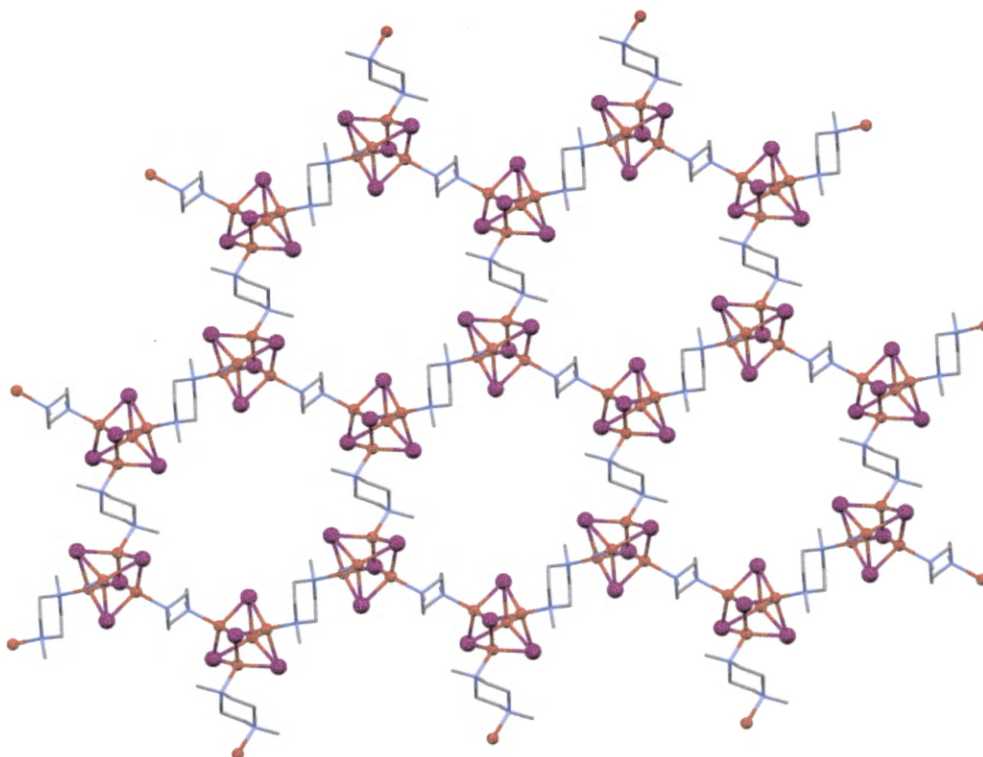


Figure 16. X-ray structure of $(\text{CuI})_4(\mathbf{7})_2$. One layer of 3-D honeycomb network shown.

Finally, all of the above compounds, $(\text{CuI})_2(\mathbf{2})$, $(\text{CuI})_2(\mathbf{4})$, $(\text{CuI})_2(\mathbf{7})$, and $(\text{CuI})_2(\mathbf{8})$, were analyzed via thermogravimetric analysis (TGA) to confirm the CuI-ligand molar ratio in the bulk products (Figure 17).

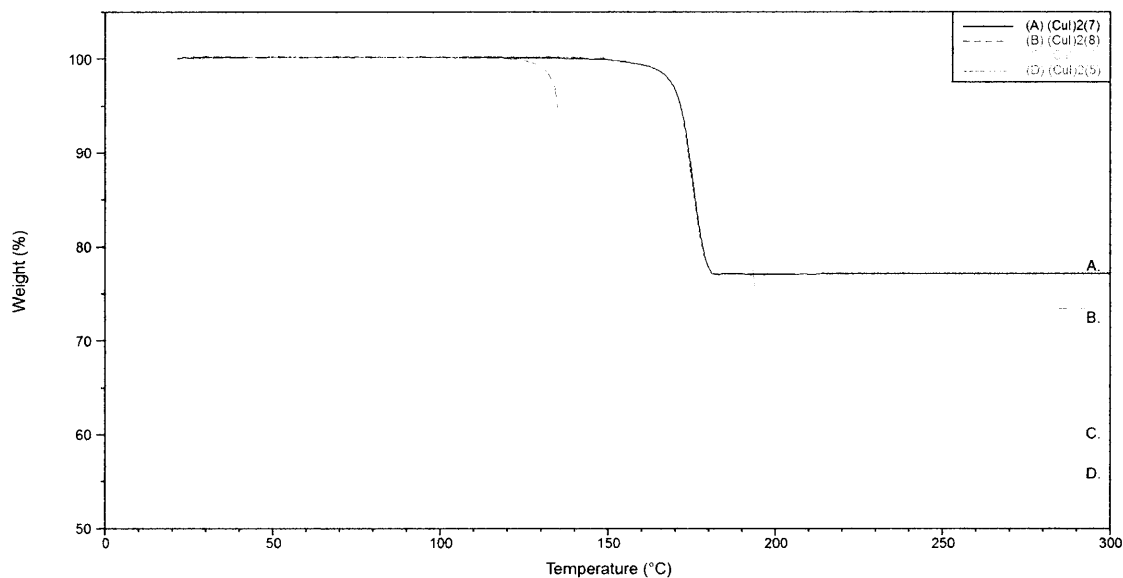


Figure 17. TGA trace for A: $(\text{CuI})_2(\mathbf{7})$, B: $(\text{CuI})_2(\mathbf{8})$, C: $(\text{CuI})_2(\mathbf{2})$, and D: $(\text{CuI})_2(\mathbf{4})$.

Table 6. TGA copper(I) iodide complexes.

Copper(I) Iodide Complexes	Theoretical Mass Loss (%)	Actual Mass Loss (%)
$(\text{CuI})_2(\mathbf{2})$	58.8	59.6
$(\text{CuI})_2(\mathbf{3})$	58.7	56.8
$(\text{CuI})_2(\mathbf{4})$	56.4	57.1
$(\text{CuI})_2(\mathbf{6})_2$	52.6	55.8
$(\text{CuI})_2(\mathbf{7})$	76.9	77.1
$(\text{CuI})_2(\mathbf{8})$	72.8	73.4
$(\text{CuI})_5(\mathbf{10})_4$	48.5	49.0
$(\text{CuI})_4(\mathbf{10})_4$	88.6/43.0	88.6/43.5

All four complexes demonstrate a single, low-temperature decomposition step between 115 and 160°C. Additionally, all of the mass losses for $(\text{CuI})_2(\mathbf{7})$, $(\text{CuI})_2(\mathbf{8})$, $(\text{CuI})_2(\mathbf{2})$, and $(\text{CuI})_2(\mathbf{4})$ were well behaved giving actual decomposition to 77.1%, 73.4%, 59.6%, and 57.1% residual mass, which compare favorably to the calculated values of 76.9%, 72.8%, 58.8%, and 56.4%, respectively (**Table 6**). A trend was noted in regard to the size of the ligand and the temperature at which the complex decomposed. The larger the ligand, the higher the temperature at which the complex decomposed, with the exception of $(\text{CuI})_2(\mathbf{7})$ for which the decomposition temperature was slightly higher, presumably because ligand **(7)** forms a three dimensional 4-coordinate copper network, which further stabilizes the overall structure.

The formation of a 3-coordinate polymer network with N,N'-dibenzylpiperazine ligand **(2)** left open the possibility that the diphenylmethyl substituent might also be used to further sterically restrict the space around Cu(I) centers. However, when reacted at room temperature a white crystalline powder was produced which, upon X-ray structural analysis was shown to consist of the type **A (Scheme 1)** 1:1 cubane structure, $(\text{CuI})_4(\mathbf{10})_4$, as shown in **Figure 18**. Furthermore, the N-diphenylmethyl substituent appears to be so large that it prevents coordination altogether due to the extremely sterically hindered N position and completely sterically free N' position, allowing ligand **10** to interact equatorially with CuI only through the N'-H group.

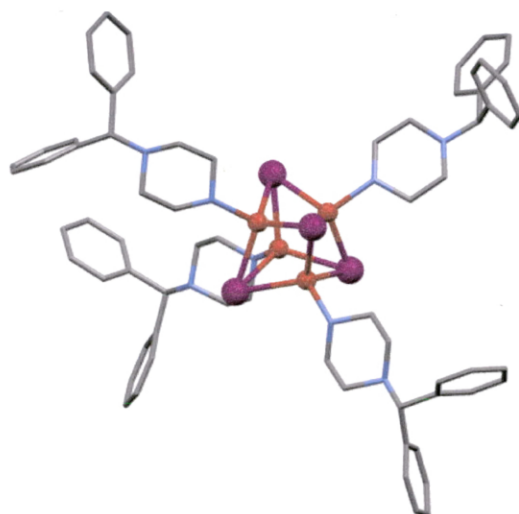


Figure 18. X-Ray Structure of $(\text{CuI})_4(\mathbf{10})_4$. Cubane tetramer.

When CuI and ligand **10** were reacted under slightly different stoichiometric conditions (2:1) a completely new structure was observed. In this complex the CuI to ligand ratio is 5:4, i.e. $(\text{CuI})_5(\mathbf{10})_4$ (**Figure 19**). This product is a yellow crystalline powder, instead of white. However, the 5:4 CuI to (**10**) ratio was not determined easily as one might gather from **Figure 19**, in which the CuI to (**10**) ratio appears to be 8:4 or 2:1.

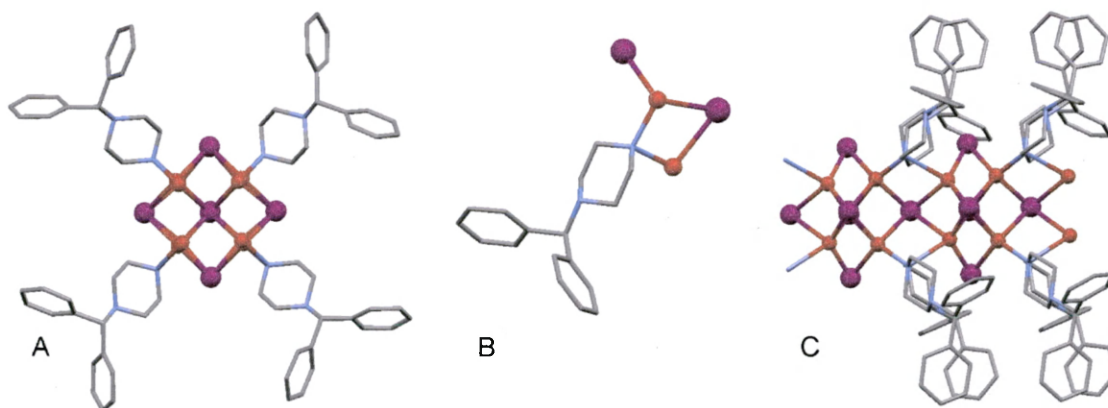


Figure 19: $(\text{CuI})_5(\mathbf{10})_4$ single crystal X-ray diffraction structures. (A) View down the c-axis, which is the 4-fold rotation axis, (B) crystallographic repeat unit, (C) view down the b-axis showing networking behavior.

In reality this molecule demonstrates an inherent limitation of single crystal X-ray diffraction. In this case there is significant disorder among the copper centers in the central metal halide cage, creating a false structural representation of $(\text{CuI})_5(\mathbf{10})_4$ wherein extra copper atoms are generated erroneously due to positional disorder about equivalent symmetry elements. Upon careful examination of the crystallographic data it was determined that significant alterations of the occupancy factors for the copper and iodine atoms would be required. The main difficulty results from the molecule lying along a 4-fold axis running down the center of the polymer chain, **Figure 19 (A)**. This creates complicated occupancy factors for the iodine atoms and disorder among the copper atoms. Since the central iodine atom (I2) lay directly on the four-fold special position, an occupancy factor of 0.25 was applied, whereas an occupancy factor of 1.00 was applied to the peripheral iodine (I1) which lies on a general position. When the 4-fold rotation is applied, the five observed iodide atoms are generated. But for the copper atoms, a large amount of disorder is present. The repeat unit contains two copper atom positions. However, only five of the eight possible copper positions generated through four-fold rotation of the repeat unit can be occupied in order to maintain the 1:1 Cu:I ratio. The particular five positions that are occupied are randomized. The illustration in **Figure 19** gives the impression that all eight copper positions are populated simultaneously, whereas in any given repeat unit only five of them are populated. To model this disorder, a total occupancy factor of 1.25 is used amongst both copper centers, yielding the needed five full copper atoms for $(\text{CuI})_5(\mathbf{10})_4$. The actual occupancies found upon refinement appear to be 0.867 for Cu1 and 0.383 for Cu2. Nevertheless, based upon the disorder and poor thermal parameters, it is also entirely possible that the copper atoms could have a total occupancy factor closer to 1.00, which would generate only four copper atoms in the repeat unit and thus a chemical formula of $(\text{Cu}_4\text{I}_5)(\mathbf{10})_4$. This is, however, believed to be unlikely because it would create an anion, and the crystal structure

does not indicate the presence of a counter ion. It is possible, of course, that one of four ligands is protonated in random fashion. This disordered proton residing on the substituted nitrogen atom would be hard to detect by X-ray. However, TGA results show a single early mass loss of 51% beginning around 202.3°C which is very similar to the calculated mass loss associated with $(\text{CuI})_5(\mathbf{10})_4$ (**Figure 20** and **Table 6**).

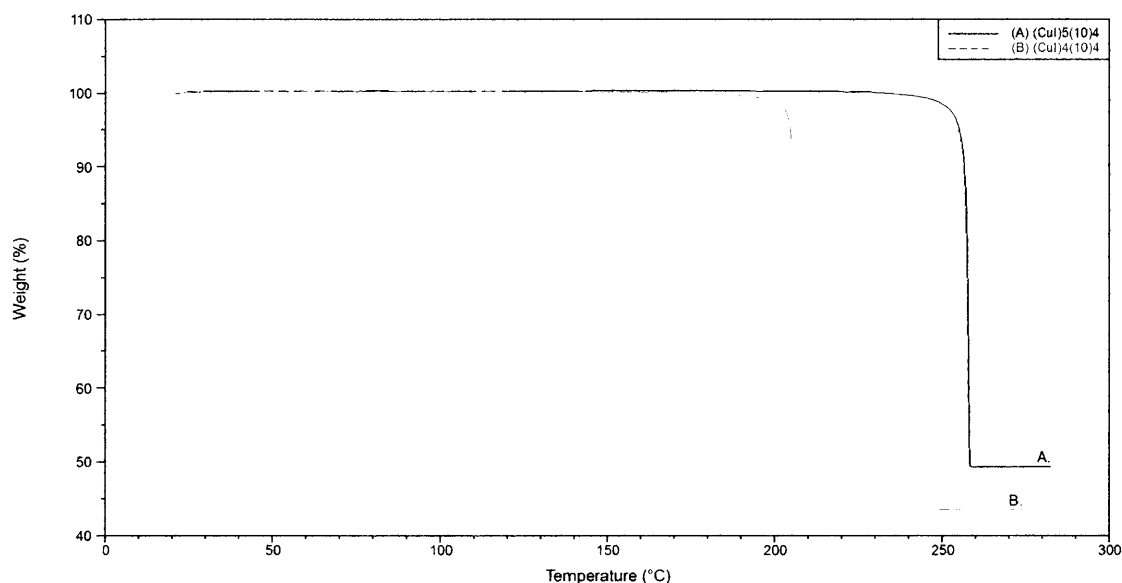


Figure 20. TGA trace of **(A)** $(\text{CuI})_5(\mathbf{10})_4$ and **(B)** $(\text{CuI})_4(\mathbf{10})_4$.

Additional examination of the TGA of the previously-discussed $(\text{CuI})_4(\mathbf{10})_4$ complex further supported these findings by revealing two significant mass plateaus at 88.6% and 44.6%. This first mass loss represents a smooth transition from the initial $(\text{CuI})_4(\mathbf{10})_4$ complex to the $(\text{CuI})_5(\mathbf{10})_4$ complex (**Figure 20 (B)**). The first thermal decomposition indicates the departure of four ligands (**10**) for every five $(\text{CuI})_4(\mathbf{10})_4$ complexes indicating conversion to $(\text{CuI})_5(\mathbf{10})_4$, corresponding to a calculated residual mass of 88.6%.



The total mass loss for the $(\text{CuI})_4(\mathbf{10})_4$ in reaction **(1)** was calculated to be 57.0%, while the actual mass change was found to be 56.7%, consistent with the 1:1 CuI to **(10)** ratio indicated by the X-ray structure.

Further exploration of the effects the diphenylmethyl substituent on CuI coordination involved the addition of a benzyl group on the opposing piperazine nitrogen, creating ligand **5**. Upon reaction with CuI, however, no appreciable coordination took place. One can deduce that even though we do observe coordination in the case of ligand **2**, the presence of the significantly larger diphenylmethyl group in addition to the benzyl group produces too much steric interference for a single Cu-N bond to form.

When the N-2-pyridylmethylpiperazines **3** and **6** were reacted with CuI, the result was the chelation products observed in **Figure 21**. Chelation results in two product forms: a polymer chain in $(\text{CuI})_2(\mathbf{3})$ and a dimer for $(\text{CuI})_2(\mathbf{6})$. The $(\text{CuI})_2(\mathbf{3})$ complex is structurally similar to the previously-discussed $(\text{CuI})_2(\mathbf{2})$ insofar as it is a polymer of linked Cu_2I_2 rhombs. However, when pyridyl-bearing ligands are present, 4-coordinate copper centers are produced due to the chelation. As a result, the polymer chains are relatively compact, with the pyridyl and piperazine groups wrapped around the copper center, preventing the formation of pendent and interdigitated R-groups such as those observed in complexes $(\text{CuI})_2(\mathbf{3})$, $(\text{CuI})_2(\mathbf{4})$, and $(\text{CuI})_2(\mathbf{5})$. Furthermore, in an attempt to force some form of polymerization with a diphenylmethyl substituent, ligand **6** was generated. However, the polymerization seen for $(\text{CuI})_2(\mathbf{3})$ is lacking when ligand **6** is used due to the bulky diphenylmethyl group sterically preventing interaction between the piperazine N and Cu. This results in the formation of the simple type **B** rhomboid dimer $(\text{CuI})_2(\mathbf{6})_2$, **Figure 21**. Crystallographically, $(\text{CuI})_2(\mathbf{6})_2$ is a half independent dimer, and for

both $(\text{CuI})_2(\mathbf{3})$ and $(\text{CuI})_2(\mathbf{6})_2$, $\text{Cu}^{\text{I}}\text{Cu}^{\text{I}}$ interactions are present (2.5673(7) and 2.6479(7) Å respectively).

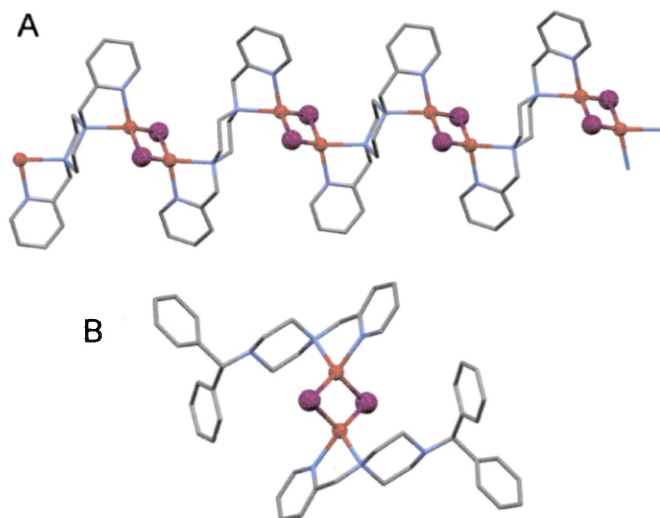


Figure 21. X-ray structures of (A) $(\text{CuI})_2(\mathbf{3})$ polymer chain and (B) $(\text{CuI})_2(\mathbf{6})$ dimer.

Different thermal stabilities were observed between these two complexes, as determined by TGA. The $(\text{CuI})_2(\mathbf{3})$ polymer chain showed a significantly lower decomposition temperature of 148°C, compared to $(\text{CuI})_2(\mathbf{6})$, which begins decomposition at 226°C, **Figure 22**. The calculated mass losses for $(\text{CuI})_2(\mathbf{3})$ and $(\text{CuI})_2(\mathbf{6})$, were determined to be 58.7% and 52.6% while the actual losses were 56.8% and 55.8% respectively, **Figure 22** and **Table 6**.

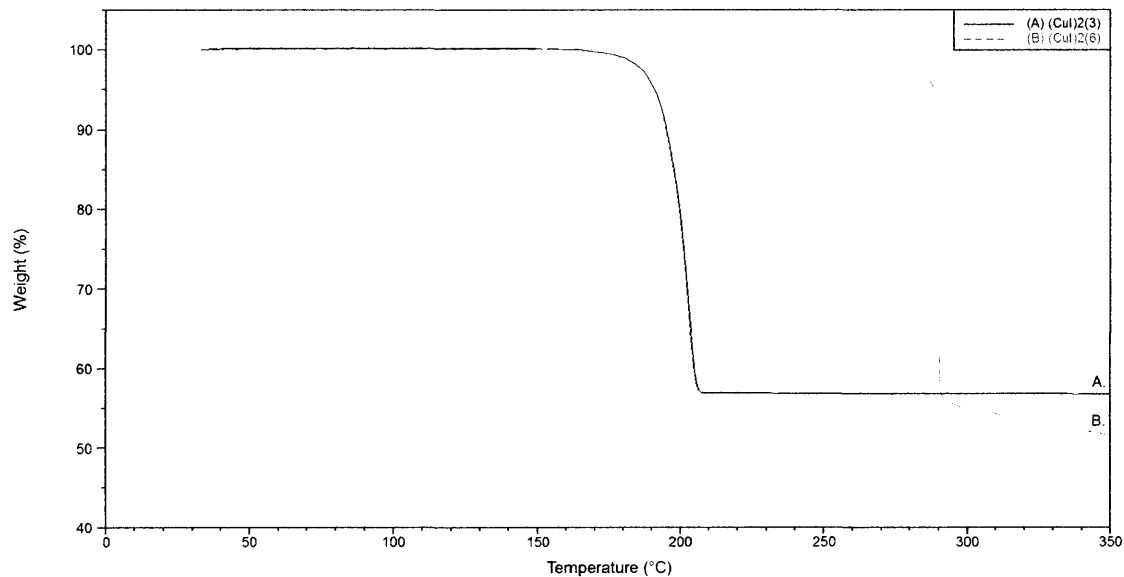


Figure 22. TGA trace of complexes **(A)** (CuI)₂(**3**) and **(B)** (CuI)₂(**6**).

Luminescence and Spectroscopy of CuI Complexes.

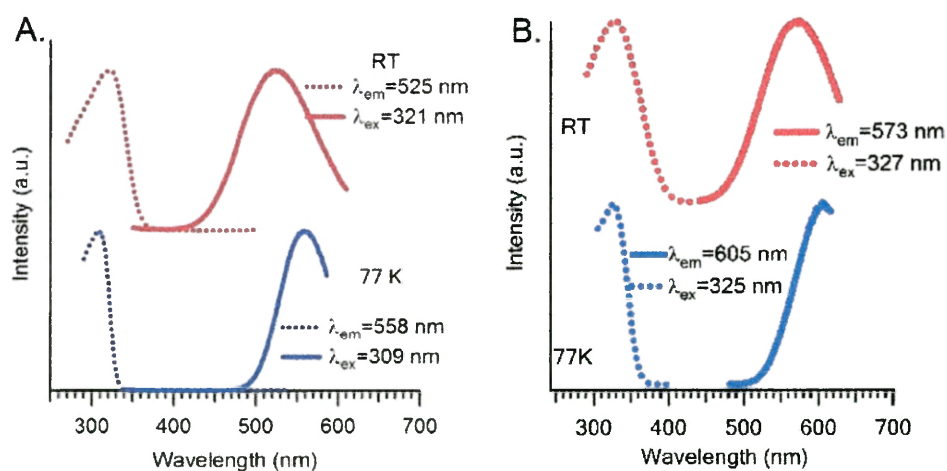
All the CuI complexes reported above were spectroscopically examined at ambient (296K) and liquid nitrogen (77K) temperatures by Prof. Howard Patterson's group at the University of Maine and were discovered to have significant luminescent properties, **Table 7**.²³ Interestingly, the most dramatic differences in the results are found between the cubane and rhomboid dimer copper(I) species. The cubanes demonstrate a low energy (LE) emission band above 500 nm, while the dimers show high energy (HE) emission features under 500 nm. Moreover, the 3-coordinate networks (**Figure 14**) demonstrated a significant ability to take up nucleophiles while also producing a new LE emission band, as is discussed below.

Table 7. CuI complex luminescence results.²³

	Temp., K	Excitation λ_{max} , nm	Emission λ_{max} , nm (colour)	Stokes Shift, cm^{-1} ^a	Lifetime, μs
(CuI) ₂ (2)	298	[non emissive]			–
	77	301	448	10900	
(CuI) ₂ (3)	298	358	496 (yellow-green)	7770	7.0, 0.7
(CuI) ₂ (4)	298	319	449 (blue)	9080	–
	77	306	447	10300	
(CuI) ₂ (6) ₂	298	358	466 (blue)	6470	–
(CuI) ₄ (7) ₂	298	321	525 (yellow)	12100	7.4
	77	309	558	14400	
(CuI) ₂ (8)	298	330	444 (blue)	7780	6.0
	77	307	438	9740	
(CuI) ₄ (10) ₄	298	327	573 (orange)	13100	20, 2.6
	77	325	605	14300	

^aCalculated between longest excitation λ_{max} and shortest emission λ_{max} .

The CuI 4-coordinate cubane complexes exhibited excitation bands centered between 320-350 nm and very broad emission bands centered in the 560-600 nm region. Furthermore, this behavior was seen for both the simple cubane (CuI)₄(**10**)₄ and the networked cubane (CuI)₄(**7**)₂ signifying that the cluster was the likely chromophore, **Figure 23**.

**Figure 23.** Luminescence excitation and emission spectra of (A) (CuI)₄(**7**)₂ and (B) (CuI)₄(**10**)₄.

Emission lifetime measurements were recorded for both species and found to be similar, with relatively long lifetimes of 7.4 and 2.6 μs respectively, indicating the phosphorescent nature of the transitions.²³ This photophysical behavior has been well documented for $(\text{CuX})_4\text{L}_4$ compounds ($X = \text{I}, \text{Br}, \text{Cl}$) and is associated with cluster centered (^3CC) transitions which are made up of two primary effects metal centered transitions (^3MC) and halide to metal charge transfer (XMCT).¹¹ Both transitions are associated with the Cu 4s orbital, which is the major contributor to the LUMO. However, XMCT relaxes from the halide-based HOMO, consisting of mainly iodide 5p orbitals in our case, to the metal-based LUMO. In contrast, the ^3MC involves transition from the largely Cu-based 3d HOMO to the LUMO. These two transitions occur simultaneously in the Cu_4I_4 clusters, and contribute significantly to the observed Stokes shifts for our two species: $(\text{CuI})_4(\mathbf{7})_2 = 12100 \text{ cm}^{-1}$ and $(\text{CuI})_4(\mathbf{10})_4 = 13100 \text{ cm}^{-1}$. This large shift is due to the relatively large reorganization required by the ^3MC , wherein contraction of the Cu_4 core and expansion of the I_4 core are necessitated by greater Cu–Cu bonding in the excited state. However, the aforementioned HE band was not observed for these two species, because the piperazine ligands are aliphatic in nature and lack the needed π/π^* system for $^3\text{XLCT}$ to take place.

The more sterically demanding piperazine ligands resulted in the formation of 3-coordinate complexes $(\text{CuI})_2(\mathbf{2})$, $(\text{CuI})_2(\mathbf{4})$, and $(\text{CuI})_2(\mathbf{8})$. These compounds were of particular interest to us because of their potential ability to react with nucleophiles in the environment with a corresponding change in emission behavior (as will be discussed below). The 3-coordinate polymer networks show strikingly different emission behavior from that of the other species in the present study. $(\text{CuI})_2(\mathbf{4})$ and $(\text{CuI})_2(\mathbf{8})$ showed peak excitation around 319 nm and sharp emission bands at 449 nm and 438 nm, respectively (**Figure 24**).

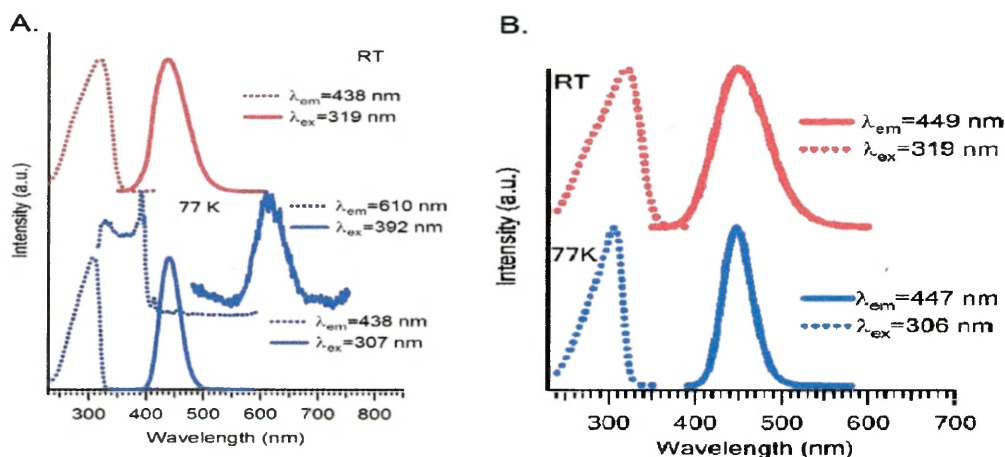


Figure 24. Luminescence excitation and emission spectra of (A) (CuI)₂(4) and (B) (CuI)₂(8).

In contrast, complex **2** only showed a luminescent response at low temperature (Figure 25). This is fairly noteworthy given the structural similarities of (CuI)₂(2) to the other 3-coordinate polymer complexes (CuI)₂(4) and (CuI)₂(8). It is believed that this phenomenon might be caused by quenching due to the above-mentioned close inter-chain phenyl-copper interactions, C6-Cu1 = 3.016 Å, resulting in a non-radiative relaxation at ambient temperature.

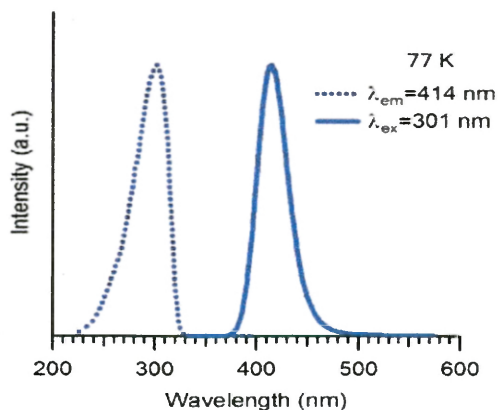


Figure 25. Luminescence excitation and emission spectra of (CuI)₂(2) which only has emission at low temperature.

Additionally, the observed Stokes shifts for all of the compounds were significantly smaller than those observed for the cubanes, being in the range between 8500-11,000 cm⁻¹. This, in turn,

indicates that excited state reorganization is still occurring, but to a lesser degree due to the simpler rhomboid dimer structure. This is still a result of the aforementioned ${}^3\text{CC}$ transitions which represent a combination of ${}^3\text{MC}$ and XMCT, but given the smaller cluster centers, there are fewer donor orbitals so the transitions are dominated by ${}^3\text{MC}$ transitions: $3\text{d}^{10} \rightarrow 4\text{s}^13\text{d}^9$.

The polymeric complex $(\text{CuI})_2(\mathbf{3})$ and the dimeric complex $(\text{CuI})_2(\mathbf{6})_2$ both contain 4-coordinate rhomboid clusters (Type **B**, **Scheme 1**) resulting from chelation by 2-pyridylmethyl piperazine group(s). Of the complexes studied, $(\text{CuI})_2(\mathbf{3})$ and $(\text{CuI})_2(\mathbf{6})_2$ showed the lowest excitation energy corresponding to wavelengths of 358 nm for both. The emission bands were found to be of moderate breadth and located at 496 nm and 466 nm (**Figure 26**), while also producing the smallest observed Stokes shifts of 7770 cm^{-1} and 6470 cm^{-1} , respectively (**Table 7**). It is important to note that these complexes are the only ones studied herein that contain aromatic ligands bound directly to the metal center. Experimental and computational studies of $(\text{CuX})_2\text{L}_4$ have revealed a variety of emission wavelengths for these luminophores. These emissions are generally associated with ${}^3\text{CC}$ transitions in the absence of pyridyl π^* -derived orbitals, and largely metal to ligand charge transfer (${}^3\text{MLCT}$) when pyridyl ligands are present.^{12,13,14,15} However the “ ${}^3\text{MLCT}$ ” transitions, in addition to having significant Cu character, the HOMO also has a lesser, but still noteworthy, iodide contribution. The relatively small Stokes shifts observed for $(\text{CuI})_2(\mathbf{3})$ and $(\text{CuI})_2(\mathbf{6})_2$ are in agreement with those previously assigned to ${}^3\text{MLCT}$ transitions, occurring between largely Cu 3d/I 5p-orbital HOMO and pyridyl π^* -derived LUMO.

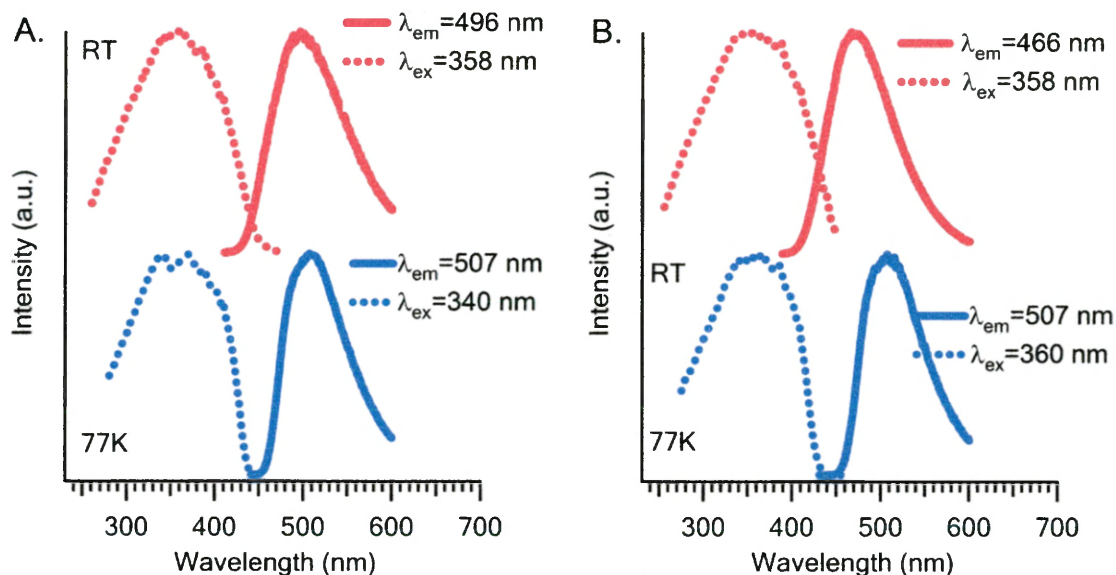


Figure 26. Luminescence excitation and emission spectra of (A) (CuI)₂(3) and (B) (CuI)₂(6).

Computational Results.

In order to further understand the photoluminescence results, computations were carried out in the lab of Prof. Craig A. Bayse at Old Dominion University, who performed Gaussian computations on the three model CuI rhomboid dimer complexes illustrated in **Figure 27**.²³ Time-dependent density functional theory (TD-DFT) was used to model both the 3-coordinate polymeric copper(I) iodide species ((CuI)₂(2), (CuI)₂(4), and (CuI)₂(8)) and the 4-coordinate chelated complexes ((CuI)₂(3) and (CuI)₂(6)). For the sake of manageable computation (CuI)₂(NMe₃)₂ (Y) was used to represent the 3-coordinate copper iodide structures and (CuI)₂(N,N'-dimethyl-2-pyridinamine) ((CuI)₂(DMP)₂, Z) took the place of the 4-coordinate chelate species (CuI)₂(3) and (CuI)₂(6). Furthermore, to compensate for the structural differences between (CuI)₂(3) and (CuI)₂(6) two different confirmations of Z, possessing C₂ and C_i symmetry, respectively, were modeled. The crystallographic data used for these models (Z₁ and Z₂) and Y are displayed in **Table 8**.

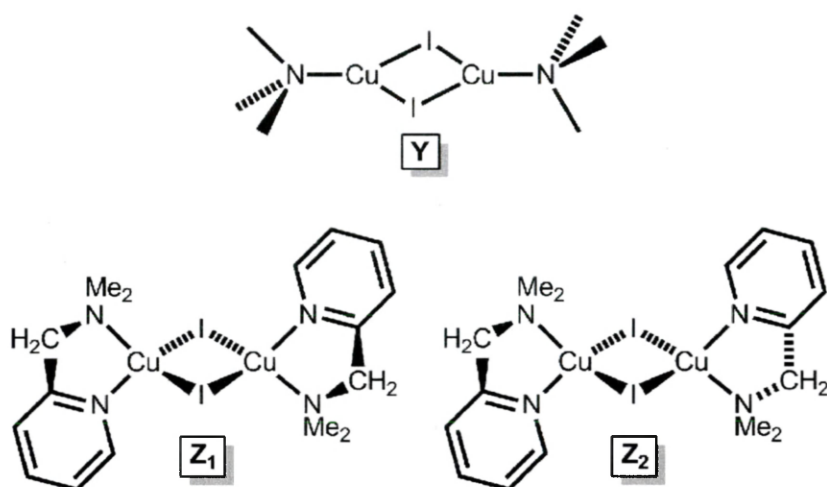


Figure 27. Computational models for the 3-coordinate CuI systems (**Y**: $(\text{CuI})_2(\text{NMe}_3)_2$) and the 4-coordinate dimer species (**Z**₁ and **Z**₂: $(\text{CuI})_2(\text{DMP})_2$).²³

Table 8. DFT bond distances and angles for the $(\text{CuI})_2(\text{NMe}_3)_2$ (**Y**) and $(\text{CuI})_2(\text{DMP})_2$ (**Z**₁ and **Z**₂) model clusters.

	Y	Z ₁	Z ₂
$d(\text{Cu}-\text{Cu}), \text{Å}$	2.487	2.538	2.538
$d(\text{X}-\text{X}), \text{Å}$	4.607	4.653	4.659
$d(\text{Cu}-\text{X}), \text{Å}$	2.598, 2.637	2.666, 2.672	2.263, 2.283
$d(\text{Cu}-\text{N}), \text{Å}$	2.062	2.082 ^a , 2.263 ^b	2.080 ^a , 2.261 ^b
$\angle(\text{Cu}-\text{X}-\text{Cu}), ^\circ$	56.7	61.5	60.2
$\angle(\text{Cu}-\text{X}-\text{Cu}), ^\circ$	123.3	122.7	122.8
q_{Cu}	0.54	0.566	0.566
q_{X}	-0.606	-0.619	-0.633
$\text{WBI}_{\text{Cu}-\text{Cu}}$	0.089		0.078
HOMO-LUMO	329 (0.023)		
HOMO-LUMO-1	272 (0.116)		
HOMO-LUMO-2		389 (0.080)	390 (0.083)

^aPyridine N. ^bAmine N.

The calculated excitation and emission properties of the 3-coordinate CuI (**Y**) species were found to be in good agreement with experimental spectroscopy of CuI materials. The

calculations indicated that two significant UV/Vis transitions were present and attributed to HOMO \rightarrow LUMO excitation at 328.6 nm and HOMO-1 \rightarrow LUMO at 271.9 nm.²³ However, the relative oscillator strengths were significantly different. It is likely that the longer wavelength XMCT HOMO \rightarrow LUMO excitation is hidden under the more intense CC HOMO-1 \rightarrow LUMO transition.

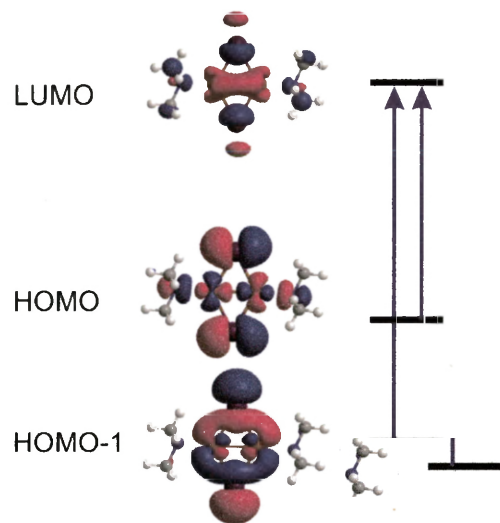


Figure 28. DFT orbitals involved in the excitation spectrum of $(\text{CuI})_2(\text{NMe}_3)_2$, **Y**.²³

Furthermore the HOMO was calculated to consist of predominately iodide p orbital character. The HOMO-1 was more unusual, consisting of fragments from the iodide p orbitals and the outer lobes of the Cu d atomic orbitals, whereas the LUMO is made up of σ bonding between the hybrid sp atomic orbitals on the Cu centers (**Figure 28**).

In the case of the 4-coordinate models **Z**₁ and **Z**₂, the significant excitations were calculated as originating from the HOMO-2 orbital, which is comparable in nature to the HOMO-

1 in **Figure 28** for the Y type species, and the LUMO, which is a π^* molecular orbital of the pyridine ring, **Figure 29**. Furthermore, this transition is attributed to a $^3\text{MLCT}$ transition.

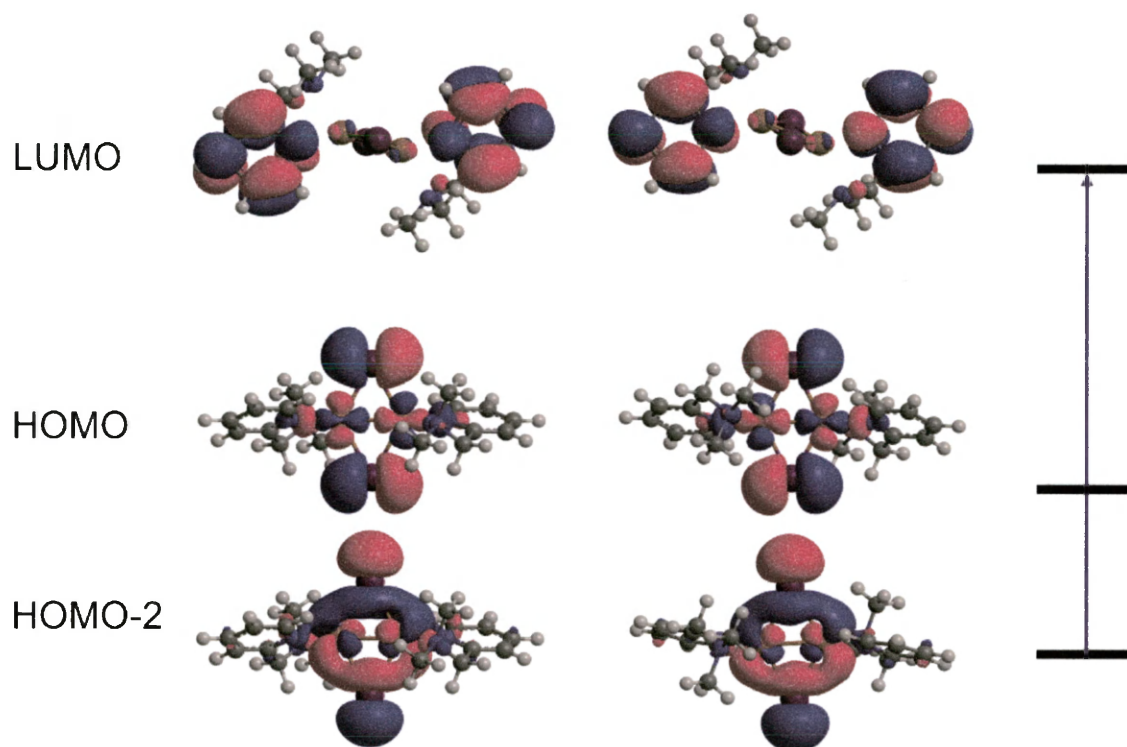


Figure 29. DFT orbitals involved in the excitation spectrum of the isomers of $(\text{CuI})_2(\text{DMP})_2$, \mathbf{Z}_1 and \mathbf{Z}_2 .²³

Vapor Exposure Studies Using $(\text{CuI})_2(\mathbf{2})$, $(\text{CuI})_2(\mathbf{4})$, and $(\text{CuI})_2(\mathbf{8})$.

The 3-coordinate networks $(\text{CuI})_2(\mathbf{3})$, $(\text{CuI})_2(\mathbf{4})$, and $(\text{CuI})_2(\mathbf{8})$ were found to be reactive toward incoming nucleophiles, including gas phase amines and sulfides. In each case, an irreversible change was observed in the luminescence emission of the copper(I) network, suggesting an interaction similar to those previously described for low-coordinate Cu(I) in CuCN and CuSCN polymers.³ In the present work, direct bonding was found between the incoming nucleophile and the copper center.^{3d,3e,20} However, in the case of the CuCN and CuSCN polymers, the Cu-Nu bonding was shown to have a reversible nature, but in the case of $(\text{CuI})_2(\mathbf{3})$,

(CuI)₂(**4**), and (CuI)₂(**8**) the irreversible nature of the emission change suggested a more significant chemical change, such as the possible replacement of ligands.

Generation of the vapor-exposed complexes was accomplished relatively simply by exposing powder samples of (CuI)₂(**2**), (CuI)₂(**4**), and (CuI)₂(**8**) to a saturated atmosphere of the various nucleophiles for ten minutes in a sealed vessel. The resulting powders were then observed under 365 nm black light to determine the extent of luminescence emission change and also to determine which Cu(I) substrate was the most responsive to the largest number of incoming nucleophiles (see **Table 9**). Of the three tested substrates, (CuI)₂(**2**) and (CuI)₂(**8**) responded to the largest number of amines and sulfides, while (CuI)₂(**4**) only responded to 12 of the 19 nucleophiles.

Table 9. Visual luminescent color data for (CuI)₂(**2**), (CuI)₂(**4**), and (CuI)₂(**8**).

Class of Nucleophile	Nucleophile	(CuI) ₂ (2) (Dark) ^a	(CuI) ₂ (4) (Blue) ^a	(CuI) ₂ (8) (Blue) ^a
Aromatics	<u>Pyridine</u>	Yellow/Green ^b	Yellow/ Orange ^b	Yellow
	<u>2-Methylpyridine</u>	Pale Blue	Yellow/Blue ^b	Blue Purple
	<u>3-Methylpyridine</u>	Orange/ yellow/green ^b	Orange/Blue ^b	Orange
	<u>2-Chloropyridine</u>	NR ^c	Dark ^d	Yellow-Orange
	<u>3-Chloropyridine</u>	Yellow	Yellow	Yellow-Green
Aliphatic	<u>Piperidine</u>	Orange	Orange	Yellow-Orange
	<u>N-Methylpiperidine</u>	yellow	Pink	Blue/Orange ^b
	<u>Morpholine</u>	Orange	Pink	Red-Orange
	<u>N-Methylmorpholine</u>	Dark ^d	Dark ^d	Dark ^d
	<u>Pyrrolidine</u>	Orange	Orange	Orange
	<u>N-Methylpyrrolidine</u>	Yellow-Orange	Orange	Orange
Sulfides	<u>Diethylamine</u>	Yellow-Orange	Orange	Orange
	<u>Tetrahydrothiophene</u>	Orange/Dark ^b	Orange	Blue/Orange ^b
	<u>Diethyl Sulfide</u>	Dark/Yellow ^b	Dark/Yellow ^b	Dark/Yellow ^b

^aBase luminescence of pure complex. ^bMottled response, ^cNo Reaction, ^dA reaction took place but formed a non luminescent product.

In response to the findings shown in **Table 7**, only substrates (CuI)₂(**2**) and (CuI)₂(**8**) were taken to the next phase of analysis wherein each exposed sample was spectroscopically analyzed for luminescence emission using the previously-described fiber optic spectrometer utilizing LED excitation at 365 nm. The resulting data are shown in **Table 10** and **Figure 30**.

Table 10. Luminescent emission data for nucleophile adducts of (CuI)₂(**2**) and (CuI)₂(**8**).

Nucleophile, Nu	(CuI) ₂ (2) Emission ^a			(CuI) ₂ (8) Emission ^a		Literature ^b
	Residual (CuI) ₂ (2) Intensity (444nm) ^d	(CuI) ₄ Nu ₄ λ _{max} ^e	(CuI) ₄ Nu ₄ Intensity ^d	(CuI) ₄ Nu ₄ λ _{max} ^e	(CuI) ₄ Nu ₄ Intensity ^d	(CuI) ₄ Nu ₄ λ _{max} ^e
Pyridine	1.00	580	7.54	581	4.80	580 ^d
2-Methylpyridine	–	482	2.83	470	9.77	–
3-Methylpyridine	0.92	590	5.88	600	0.99	588
2-Chloropyridine	<0.2	–	<0.2	–	<0.2	–
3-Chloropyridine	<0.2	554	4.24	553	2.84	537 ^c
Piperidine	1.57	600	1.88	580	3.40	590 ^d
N-Methylpiperidine	2.10	568	0.32	565	0.46	–
Morpholine	1.25	655	1.15	654	2.07	625 ^d
N-Methylmorpholine	1.92	–	<0.2	–	<0.2	–
Pyrrolidine	0.51	640	0.93	642	1.10	–
N-Methylpyrrolidine	<0.2	610	5.20	608	1.20	–
Diethylamine	<0.2	619	6.12	609	0.76	–
Diethyl sulphide	1.60	559	0.47	552	0.94	–
Tetrahydrothiophene	2.00	–	<0.2	666	0.38	–

^aSolid state, 298 K. ^bRef. 12a. ^cIn toluene, 298 K. ^dx10⁻³ μW/cm²/nm. ^enm

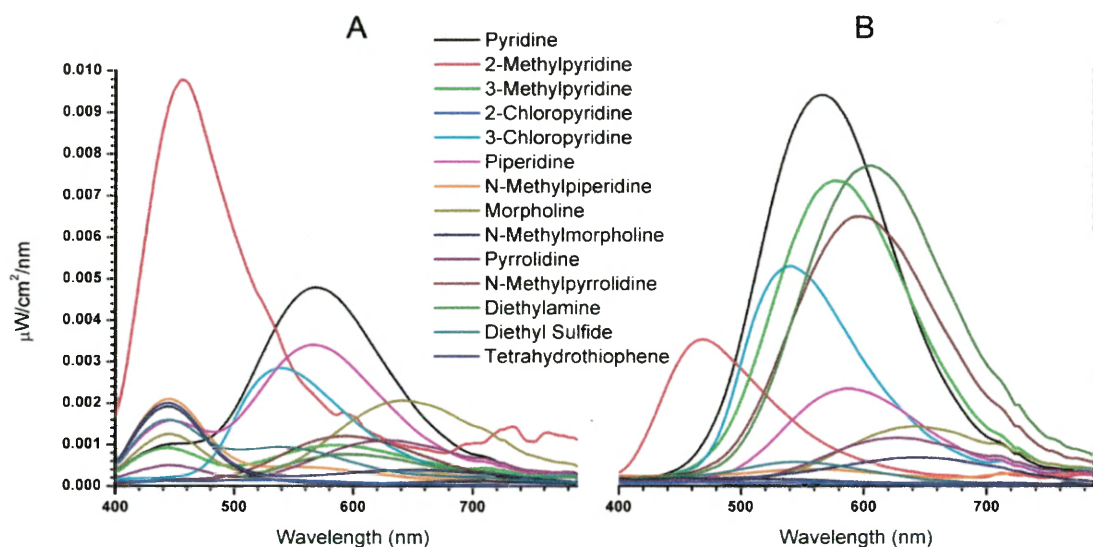


Figure 30. Emission spectra of $(\text{CuI})_2(\mathbf{8})$ (A) and $(\text{CuI})_2(\mathbf{2})$ (B) after exposure to various Nu's (365 nm excitation).

In reviewing these data, a few important anomalies were noted, beginning with $(\text{CuI})_2(\mathbf{8})$, which showed both a consistent high energy (HE) response at 444 nm and a variable low energy (LE) emission. The HE emission was attributed to the presence of unreacted $(\text{CuI})_2(\mathbf{8})$ substrate which features an emission at around 444 nm in its unexposed form (**Table 7**). In contrast, the LE emission was ascribed to reaction of the nucleophile with the substrate, generating a characteristic emission unique to that nucleophile. An interesting consequence of the simultaneous HE and LE emission can be observed in **Figure 31** wherein a mottled color is observable as a result of the dual emissions. Furthermore, the HE band associated with $(\text{CuI})_2(\mathbf{8})$ also serves as a marker for unreacted substrate during vapor exposure, see **Table 10**. In all cases, the HE emission was at least diminished and sometimes extinguished completely, such as in the cases of Nu = pyridine, 2-chloropyridine, and 3-chloropyridine. Interestingly, in the case of Nu = 2-chloropyridine, emission associated with $(\text{CuI})_2(\mathbf{8})$ was completely extinguished, whereas no LE emission band associated with 2-chloropyridine was observed. The apparent lack

of emission in the vapor-exposed product was therefore considered to be the formation of products that were non-emissive at room temperature.

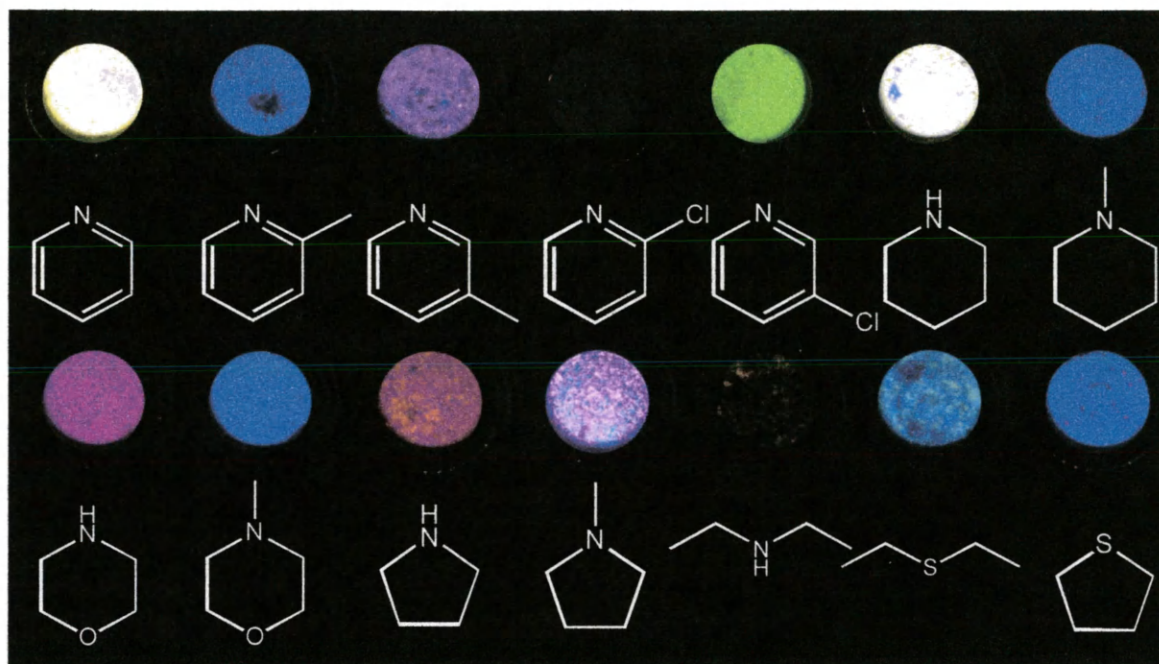


Figure 31. Luminescence response of Nu-exposed $(\text{CuI})_2(\mathbf{8})$ under 365 nm excitation.

In contrast, the nucleophile exposure adducts of $(\text{CuI})_2(\mathbf{2})$ showed only a single LE emission. This emission must be attributed to the nucleophile adducts, because pure $(\text{CuI})_2(\mathbf{2})$ substrate lacks a luminescent response, avoiding the dual emission and mottled luminescence observed for $(\text{CuI})_2(\mathbf{8})$, see **Figure 32**.

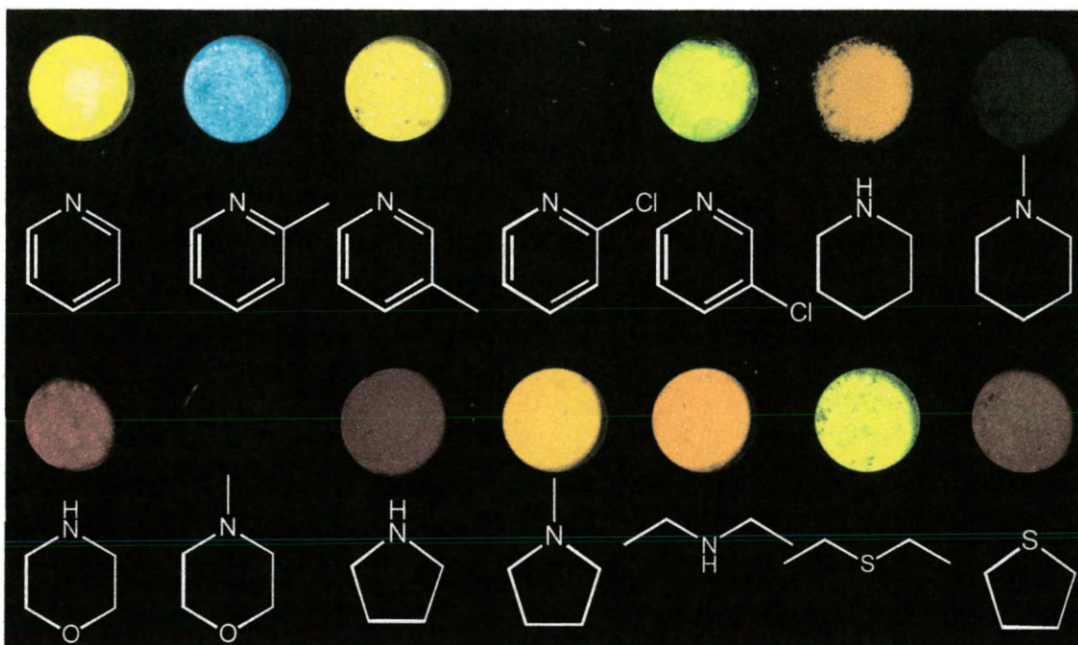
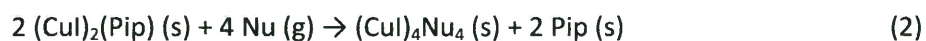


Figure 32. Luminescence response of Nu-exposed $(\text{CuI})_2(\mathbf{2})$ under 365 nm excitation.

Interestingly, upon close inspection, the LE emissions for each particular nucleophile were found to be essentially identical for both Cu(I) substrates (see **Table 10**). This observation suggests that a common Cu(I) complex was being generated for both $(\text{CuI})_2(\mathbf{2})$ and $(\text{CuI})_2(\mathbf{8})$. It was further noted that the emission wavelengths of the adduct species were in good agreement with the emissions of $(\text{CuI})_4\text{Nu}_4$ cubane species that had been previously reported.¹² Consistent with these findings, it is proposed that the CuI-piperazine chains were not being decorated with the nucleophiles as initially thought, but rather the nucleophiles were disrupting sections of the $(\text{CuI})_2(\mathbf{2}/\mathbf{8})$ polymer chains and generating new $(\text{CuI})_4\text{Nu}_4$ cubanes with release of piperazine ligand, as described in reaction (2) (Pip = **2** or **8**).



X-ray Powder Diffraction.

Powder X-ray diffraction (PXRD) was performed on all the bulk reaction products of CuI and substituted piperazines. The resulting data were compared to the calculated powder patterns generated from single crystal X-ray results. Mismatches were observed for $(\text{CuI})_2(\mathbf{3})$ and $(\text{CuI})_2(\mathbf{4})$ despite the fact that the stoichiometries of the bulk and crystal products were identical, implying polymorphism (**Figure 33**). However, this is not surprising given the fact that six polymorphs are known for $(\text{CuI})_4(\text{DABCO})_2$.^{7,8}

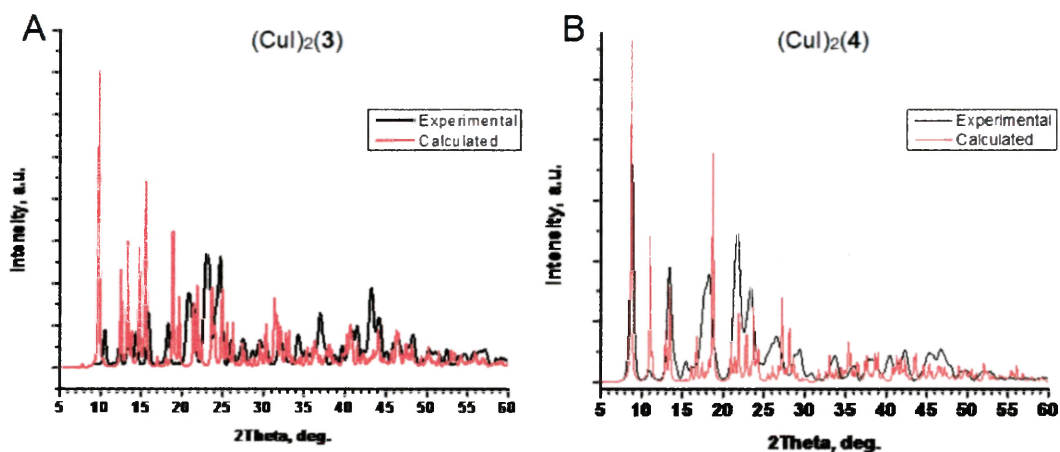


Figure 33. Experimental and calculated X-ray powder diffractograms of (A) $(\text{CuI})_2(\mathbf{3})$ and (B) $(\text{CuI})_2(\mathbf{4})$.

Nevertheless, in the case of complexes $(\text{CuI})_2(\mathbf{2})$, $(\text{CuI})_2(\mathbf{6})$, $(\text{CuI})_2(\mathbf{8})$, and $(\text{CuI})_2(\mathbf{10})$, good PXRD matches to the calculated powder patterns were found (**Figure 34**).

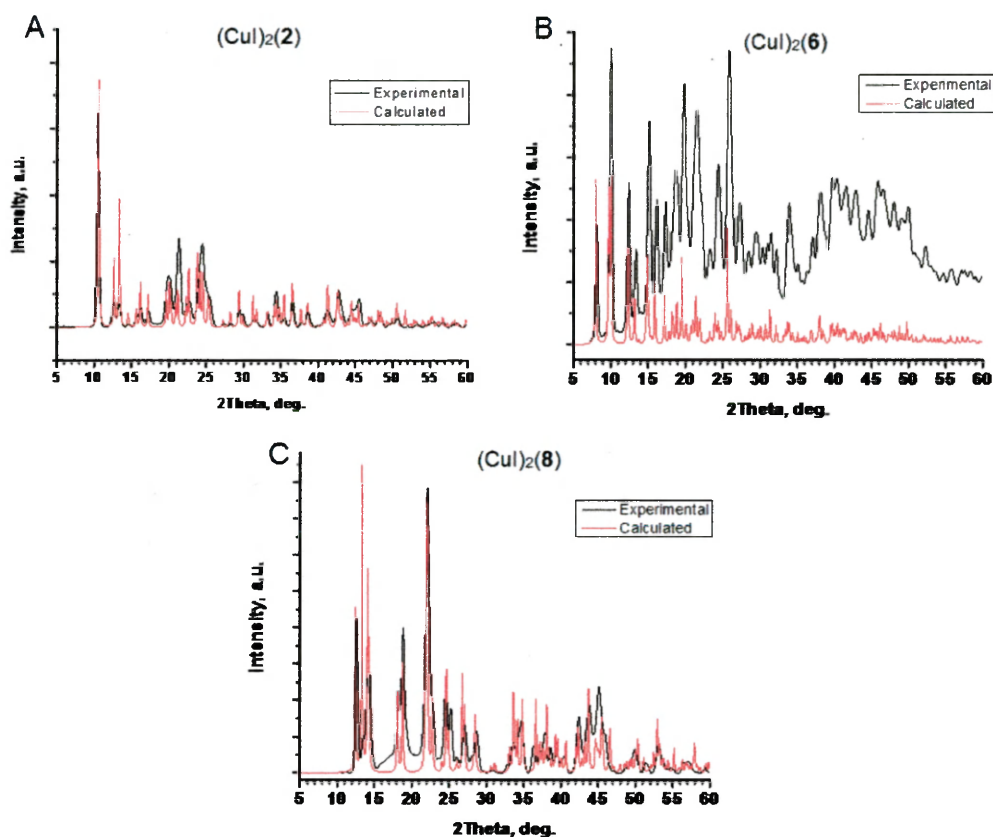


Figure 34. Experimental and calculated X-ray powder patterns for (A) $(\text{CuI})_2(\mathbf{2})$, (B) $(\text{CuI})_2(\mathbf{6})$, and (C) $(\text{CuI})_2(\mathbf{8})$.

Finally, PXRD was also used to confirm the nucleophile-induced conversion of the CuI-piperazine polymer to the CuI-Nu tetramers. This was done by suspending a sample of solid $(\text{CuI})_2(\mathbf{8})$ in a 5% pyridine/toluene solution and then stirring the mixture for two hours at room temperature. The resulting powder was then filtered. PXRD of this powder revealed the complete conversion of the $(\text{CuI})_2(\mathbf{8})$ to $(\text{CuI})_4\text{Py}_4$, as confirmed by comparison to PXRD pattern of an authentic sample of the $(\text{CuI})_4\text{Py}_4$ (**Figure 35**).

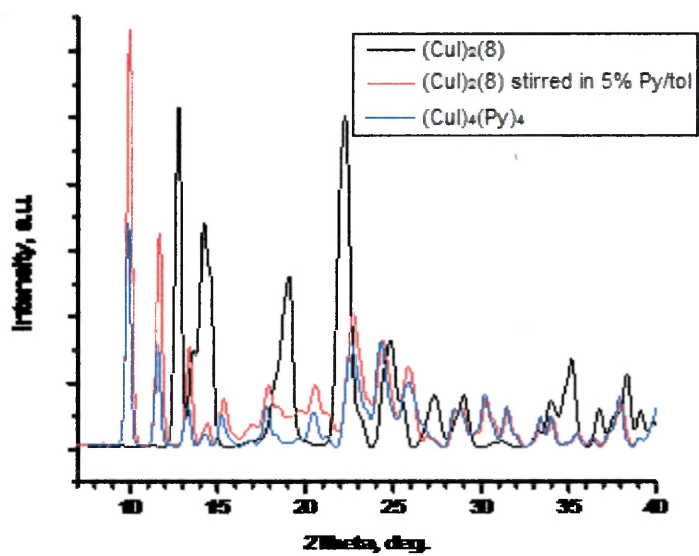


Figure 35. X-ray powder diffraction comparison of unreacted $(\text{CuI})_2(\mathbf{8})$ (black trace), $(\text{CuI})_2(\mathbf{8})$ stirred in 5% pyridine/toluene for two hours (red trace), and $(\text{CuI})_4\text{Py}_4$ (blue trace), showing the conversion of $(\text{CuI})_2(\mathbf{8})$ to $(\text{CuI})_4\text{Py}_4$ on exposure to Py.

CONCLUSION

We have herein evaluated the effects of various disubstituted piperazine ligands upon the complexation and luminescent properties of CuI, in the hopes of designing a luminescent substrate that could be used to detect the presence of different gaseous amines and sulfides. Various piperazine-based ligands were purchased (**7-10**) or generated through simple reductive amination chemistry (**1-6**). In turn each ligand was tested to see whether and how it would react with CuI. A CuI complex was generated for ligands **2, 3, 4, 6, 7, 8, and 10**, all of which had significant luminescent properties, forming either 3-coordinate polymeric complexes ((CuI)₂(**2**), (CuI)₂(**4**), (CuI)₂(**8**)), 4-coordinate dimers or rhomboid polymers ((CuI)₂(**3**), (CuI)₂(**6**)), or 4-coordinate cubane tetrameric/polymeric complexes ((CuI)₂(**7**), (CuI)₂(**10**)). Of those seven, only (CuI)₂(**2**), (CuI)₂(**4**), and (CuI)₂(**8**) produced a viable 3-coordinate complex that was readily reactive to incoming gaseous amines and sulfides. Whereas the other four complexes generated 4-coordinate species that lacked an open coordination site for nucleophilic attack.

However, all seven complex species produced some form of luminescent response that was attributed to ³CC transitions, ³MC transitions, ³XLCT, and ³MLCT, depending on the structural make up of the complex. For the 3-coordinate polymer species, mainly ³MC transitions and ³XLCT were exhibited. However, when the 4-coordinate rhomboid dimer or polymer complexes were investigated the photophysical activity was attributed to ³CC and ³MLCT. Finally, the cubane based structures possessed luminescent activity as a result of ³CC, ³MC, and ³XLCT.

The three 3-coordinate complexes that were found to be receptive to gaseous nucleophiles were then further tested against a gamut of amines and sulfides to determine the

range of accessible reactivity. $(\text{CuI})_2(\mathbf{2})$, $(\text{CuI})_2(\mathbf{4})$, and $(\text{CuI})_2(\mathbf{8})$ showed good sensitivity to the tested amines and sulfides, resulting in product powders that luminesced at specific wavelengths characteristic of the particular amine or sulfide used. However, due to overlapping luminescent peaks resulting from residual substrate, complexes $(\text{CuI})_2(\mathbf{4})$, and $(\text{CuI})_2(\mathbf{8})$ were eliminated as viable detector substrates because each possessed its own luminescent characteristics at room temperature. However, $(\text{CuI})_2(\mathbf{2})$ was found to be non-luminescent at room temperature, and when exposed to the gaseous nucleophiles a single luminescent response was seen which was attributed only to the portion that reacted with the nucleophile.

Upon careful investigation, it was found that the luminescence resulting from exposure of $(\text{CuI})_2(\mathbf{2})$, $(\text{CuI})_2(\mathbf{4})$, and $(\text{CuI})_2(\mathbf{8})$ was directly attributable to formation of cubane product $(\text{CuI})_4\text{Nu}_4$, with concomitant loss of piperazine ligand. It was determined that $(\text{CuI})_2(\mathbf{2})$ would provide the best substrate for small molecule detection, because of its reaction with the widest variety of amines and sulfides, along with its lack of luminescence emission at room temperature, providing a relatively simple, if irreversible, emission response.

REFERENCES

- 1) EPA, Definition of Volatile Organic Compounds (VOC).
http://www.epa.gov/ttn/naaqs/ozone/ozonetech/def_voc.htm
- 2) J. David, S. M. Scott, Z. Ali, W. T. O'Hare. *Microchim. Acta.* (2005) **149**, 1-17.
- 3) (a) T. A. Tronic, K. E. deKrafft, M. J. Lim, A. N. Ley, R. D. Pike, *Inorg. Chem.* 2007, **46**, 8897–8912. (b) R. D. Pike, K. E. deKrafft, A. N. Ley, T. A. Tronic, *Chem. Commun.* 2007, 3732–3734. (c) M. J. Lim, C. A. Murray, T. A. Tronic, K. E. deKrafft, A. N. Ley, J. C. deButts, R. D. Pike, H. Lu, H. H. Patterson, *Inorg. Chem.* 2008, **47**, 6931–6947. (d) A. N. Ley, L. E. Dunaway, T. P. Brewster, M. D. Dembo, T. D. Harris, F. Baril-Robert, X. Li, H. N. Patterson, R. D. Pike, *Chem. Commun.* 2010, **46**, 4565–4567. (e) M. D. Dembo, L. E. Dunaway, J. S. Jones, E. A. Lepekhina, S. M. McCullough, J. L. Ming, X. Li, F. Baril-Robert, H. H. Patterson, C. A. Bayse, R. D. Pike, *Inorg. Chim. Acta* 2010, **364**, 102–114.
- 4) M. E. Chapman, P. Ayyappan, B. M. Foxman, G. T. Yee, W. Lin. *Crystal Growth & Design.* 2001, **1**, 161-163.
- 5) H. Lin, B. Mu, X. wang, A. Tain. *Journal of Organometallic Chemistry.* 2012, **702**, 36-44.
- 6) (a) C.L.Raston, A.H.White, *J.Chem.Soc.,Dalton Trans.*, 1976, 2153-2156. (b) J.C.Dyason, L.M.Engelhardt, P.C.Healy, A.H.White, *Aust.J.Chem.* 1984, **37**, 2201. (c) E.Eitel, D.Oelkrug, W.Hiller, J.Strahle, *Z.Naturforsch.,B:Chem.Sci.* 1980, **35**, 1247. (d) P.C.Healy, C.Pakawatchai, C.L.Raston, B.W.Skelton, A.H.White, *J. Chem. Soc., Dalton Trans.*, 1983, 1905-1916. (e) J.A.Campbell, C.L.Raston, A.H.White, *Aust.J.Chem.* 1977, **30**, 1937.
- 7) (a) M. Bi, G. Li, J. Hua, X. Liu, Y. Hu, Z. Shi, S. Feng, *CrystEngComm* 2007, **9**, 984–986. (b) M. Bi, G. Li, Y. Zou, Z. Shi, S. Feng, *Inorg. Chem.* 2007, **46**, 604–606. (c) M. Bi, G. Li, J. Hua, Y. Liu, X. Liu, Y. Hu, Z. Shi, S. Feng, *Cryst. Growth Des.* 2007, **7**, 2066–2070. (d) D. Braga, L. Maini, P. P. Mazzeo, B. Ventura, *Chem. Eur. J.* 2010, **16**, 1553–1559. (e) Y. Zhang, T. Wu, R. Liu, T. Dou, X. Bu, P. Feng, *Cryst. Growth Des.* 2010, **10**, 2047–2049.
- 8) A. J. Blake, N. R. Brooks, N. R. Champness, M. Crew, A. Deveson, D. Fenske, D. H. Gregory, L. R. Hanton, P. Hubberstey, M. Schröder, *Chem. Commun.* 2001, 1432–1433. (b) S. Hu, M.-L. Tong, *Dalton Trans.* 2005, 1165–1167. (c) T. H. Kim, K. Y. Lee, Y. W. Shin, S.-T. Moon, K.-M. Park, J. S. Kim, Y. Kang, S. S. Lee, J. Kim, *Inorg. Chem. Commun.* 2005, **8**, 27–30. (d) J. Wang, S.-L. Zheng, S. Hu, Y.-H. Zhang, M.-L. Tong, *Inorg. Chem.* 2007, **46**, 795–800. (e) T. H. Kim, Y. W. Shin, J. H. Jung, J. S. Kim, J. Kim, *Angew. Chem., Int. Ed.* 2008, **47**, 685–688. (f) C. Xie, L. Zhou, W. Feng, J. Wang, W. Chen, *J. Mol. Struct.* 2009, **921**, 132–136. (g) Z.-G. Zhao, J. Zhang, X.-Y. Wu, Q.-G. Zhai, L.-J. Chen, S.-M. Chen, Y.-M. Xie, C.-Z. Lu, *CrystEngComm* 2008, **10**, 273–275. (h) M.-C. Hu, Y. Wang, Q.-G. Zhai, S.-N. Li, Y.-C. Jiang, Y. Zhang, *Inorg. Chem.* 2009, **48**, 1449–1468. (i) T. Li, S.-W. Du, *J. Cluster Sci.* 2008, **19**, 323–330. (j) Y. Chen, H.-X. Li, D. Liu, L.-L. Liu, N.-Y. Li, H.-Y. Ye, Y. Zhang, J.-P. Lang, *Cryst. Growth Des.* 2008, **8**, 3810–3816. (k) T. H. Kim, Y. W. Shin, J. H. Jung, J. S. Kim, J. Kim *Angew. Chem. Int. Ed.* 2008, **47**, 685–688. (l) M. Knorr, F. Guyon, A. Khatyr, C. Daschlein, C. Strohmam, S. M. Aly, A. S. Abd-El-Aziz, D. Fortin, P. D. Harvey, *Dalton Trans.*

2009, 948–955. (m) L.-L. Li, H.-X. Li, Z.-G. Ren, D. Liu, Y. Chen, Y. Zhang, J.-P. Lang, *Dalton Trans.* 2009, 8567–8573. (n) T. H. Kim, Y. W. Shin, S. S. Lee, J. Kim, *Inorg. Chem. Commun.* 2007, **10**, 11–14. (o) C. Xie, L. Zhou, W. Feng, J. Wang, W. Chen *J. Mol. Struct.* 2009, **921**, 132–136. (p) X. Chai, S. Zhang, Y. Chen, Y. Sun, H. Zhang, X. Xu, *Inorg. Chem. Commun.* 2010, **13**, 240–243. (q) M. Knorr, F. Guyon, M. M. Kubicki, Y. Rousselin, S. M. Aly, P. D. Harvey, *New J. Chem.* 2011, **35**, 1184–1188.

9) (a) B. Rossenbeck, W. S. Sheldrick, C. Näther, *Z. Naturforsch.* 2000, **55b**, 467–472. (b) C. Näther, I. Jess, *Inorg. Chem.* 2002, **4**, 813–820. (c) T. Kromp, W. S. Sheldrick, C. Näther, *Z. Anorg. Allg. Chem.* 2003, **629**, 45–54. (d) R. D. Pike, B. A. Reinecke, M. E. Dellinger, A. B. Wiles, J. D. Harper, J. R. Cole, K. A. Dendramis, B. D. Borne, J. L. Harris, W. T. Pennington, *Organometallics* 2004, **23**, 1986–1990. (e) D. Braga, F. Grepioni, L. Maini, P. P. Mazzeoa, B. Ventura, *New J. Chem.* 2011, **35**, 339–344.

10) P. M. Graham, R. D. Pike, M. Sabat R. D. Bailey, W. T. Pennington, *Inorg. Chem.* 2000, **39**, 5121–5132, and references cited therein. (b) C. Näther, I. Jess, *J. Solid State Chem.* 2002, **169**, 103–112. (b) C. Näther, I. Jess, *Z. Naturforsch.* 2002, **57b**, 1133–1140. (c) C. Näther, M. Wreidt, I. Jess, *Inorg. Chem.* 2003, **42**, 2391–2397. (d) C. Näther, I. Jess, *Inorg. Chem.* 2003, **42**, 2968–2976.

11) Q. Hou, J.-H. Yu, J.-N. Xu, Q.-F. Yang, J.-Q. Xu, *Inorg. Chim. Acta* 2009, **362**, 2802–2806.

12) (a) Ford, Peter C. *Chem. Rev.* **1999**, *99*, 3625–3647. (b) M. Vitale, C. K. Ryu, W. E. Palke, P. C. Ford, *Inorg. Chem.* 1994, **33**, 561–566. (c) P. Aslanidis, P. J. Cox, S. Divanidis, A. C. Tsipis, *Inorg. Chem.* 2002, **41**, 6875–6886. (d) H. Araki, K. Tsuge, Y. Sasaki, S. Ishizaka, N. Kitamura, *Inorg. Chem.* 2005, **44**, 9667–9675. (e) Z. Liu, P. I. Djurovich, M. T. Whited, M. E. Thompson, *Inorg. Chem.* 2012, **51**, 230–236.

13) SMART Apex II, Data Collection Software, version 2.1; Bruker AXS Inc.: Madison, WI, 2005.

14) SAINT Plus, Data Reduction Software, version 7.34a; Bruker AXS Inc.: Madison, WI, 2005.

15) Sheldrick GM (2008) *Acta Crystallogr., Sect. A* **64**: 112–122.

16) Zhang M, Zhou Y-H, Hou L-H, Yang X-H. *Acta Crystallogr.* 2010, Sect. E **66**: o3336.

17) Ratilainen J, Airola K, Fröhlich R, Nieger M, Rissanen K, *Polyhedron.* 1999, **18**: 2265–2273.

18) (a) Owston PG, Peters R, Ramsammy E, Tasker PA, Trotter J. *J. Chem. Soc., Chem. Commun.* 1999, 1218–1220. (b) Gourdon A, Launay J-P, Bujoli-Doeuff M, Heisel F, Miehe J-A, Amouyal E, Boillet M-L. *J. Photochem. Photobiol.* 1993, **71**, 13–25. (c) Spange S, El-Sayed M, Muller H, Rheinwald G, Lang H, Poppitz W. *Eur. J. Org. Chem.* 2002, 4159–4168. (d) MacPhee JM, Guzman HL, Almarsson O. *J. Am. Chem. Soc.* 2003, **125**, 8456–8457. (e) Lynch DE, McClenaghan I. *Acta Crystallogr.*, 2004, *Sect. C* **60**: o1–o5. (f) Cherkasov V, Druzhkov N, Kocherova T, Fukin G, Shavyrin A. *Tetrahedron.* 2011, **67**, 80–84.

19) (a) Naveen S, Swamy SN, Basappa B, Rangappa KS. *Anal. Sci.* 2006, **22**, 41–42. (b) Kumar CSA, Prasad SBB, Thimmegowda NR, Rangappa KS, Chandrappa S, Naveen S, Sridhar MA, Prasad JS. *Mol. Cryst. Liq. Cryst.* 2007, **469**, 111–119. (c) Vinaya K, Naveen S, Kumar CSA, Benakaprasad SB, Sridhar MA, Prasad JS, Rangappa KS. *Struct. Chem.* 2008, **19**, 765–770. (d) Amor FB, M'hamed MO, Mrabet H, Driss A, Efrif ML

Acta Crystallogr., 2008, *Sect. E* 64, o1872. (e) Naveen S, Kumar CSA, Prasad SBB, Vinaya K, Prasad JS, Rangappa KS. *J. Chem. Cryst.* 2009, **39**, 395–398. (f) Naveen S, Kumar CSA, Manjunath HR, Prasad SBB, Sridhar MA, Rangappa KS, Prasad JS. *Mol. Cryst. Liq. Cryst.* 2009, **503**, 151–158.

20) (a) G.L. Soloveichik, O. Eisenstein, J.T. Poulton, W.E. Streib, J.C. Huffman, K.G. Caulton, *Inorg. Chem.* 1992, **31**, 3306–3312 (b) A. Carvajal, X.-Y. Liu, P. Alemany, J.J. Novoa, S. Alvarez, *Int. J. Quant. Chem.* 2002, **86**, 100–105.

21) Halfen JA, Uhan JM, Fox DC, Mehn (MP), Que, Jr. L (2000) *Inorg. Chem.* **39**: 4913–4920.

22) M.Munakata, T.Kuroda-Sowa, M.Maekawa, A.Honda, S.Kitagawa. *J. Chem. Soc., Dalton Trans.*, (1994), 2771-2775.

23) Jason P. Safko, Jacob E. Kuperstock, Shannon M. McCullough, Andrew M. Noviello, Robert D. Pike, Craig A. Bayse, Xiaobo Li, James P. Killarney, Caitlin Murphy, and Howard H. Patterson, to be submitted.